Nanofabrication (2022) 7, 280-313
https://doi.org/10.37819/nanofab.007.189

REVIEW ARTICLE

Graphitic carbon nitride-based upconversion photocatalyst for hydrogen production and water purification

Anita Sudhaik[a], Pankaj Raizada[a], Aftab Aslam Parwaz Khan[b], Arachana Singh[c], Pardeep Singh[a,*]

[a]*School of Advanced Chemical Sciences, Faculty of Basic Sciences, Shoolini University, Solan (HP), India—173229*
[b]*Center of Excellence for Advanced Materials Research, King Abdulaziz University, P.O. Box 80203, Jeddah 21589, Saudi Arabia*
[c]*Advanced Materials and Processes Research Institute, Hoshangabad Road, Bhopal (MP), India. 462026*
**Corresponding author: pardeepchem@gmail.com*

ABSTRACT

Upconversion luminescence (UCL) is mainly a nonlinear optical method that some engineered nanomaterials can attain and helps in the transformation of low energy phonons (near-infrared photons) into higher energy phonons (ultraviolet (UV) and visible light photons). Upconversion (UC) nanomaterials are a suitable candidate for preparing near-infrared (NIR) light-responsive photocatalytic systems by mixing with other photocatalysts. Many reports have been published on lanthanide-based UC materials (Ln^{3+} ions as dopants) and carbon quantum dots (CQDs) carrying UC property with their use in photocatalytic removal of pollutants and energy production. Besides these UC nanomaterials, graphitic carbon nitride (g-C_3N_4) as a potential photocatalyst (metal-free and ecofriendly) has gained attention owing to its unique and amazing possessions. But some limitations and inadequate utilization of visible light restrict its photocatalytic applicability. Therefore, to enhance or widen its light-harvesting property towards the NIR region, the integration of upconversion nanocrystals (UC NCs) into g-C_3N_4 is considered an effective approach. Thus, the present review is focused on the amalgamation of g-C_3N_4 with UC nanomaterials for full solar spectrum absorption in H_2 production and pollutant degradation via NIR light absorption.

ARTICLE HISTORY
Received: 26-11-2021
Revised: 16-01-2022
Accepted: 19-01-2022

KEYWORDS
Graphitic carbon nitride
NIR photocatalysis
Upconversion
H_2 production
Pollutant degradation

1. Introduction

Nowadays, energy scarcity and environmental problems have strengthened the attentiveness of the scientific community worldwide [1-4]. To resolve these major issues, solar energy is the most available reusable energy source [5-7]. Among all, photocatalysis (an advanced oxidation technique and a solar light-assisted process) is more favorable and advantageous for tackling energy and environment-related problems by the direct harnessing of solar energy [8-10]. In this field, fabrication and utilization of capable, harmless, and viable semiconductor photocatalysts have fascinated the devotion of researchers in solar energy conversion (H_2 production, CO_2 reduction), bacterial disinfection, and environmental remediation [11-13]. Since 1972, the finding of TiO_2 as a photocatalytic material in water splitting has grabbed the concentration of scientists in the photocatalysis field [6, 10, 14-16]. Photocatalysis caused the generation of photocarriers in semiconductors under solar light irradiation [17-19]. The generated charge carriers during the photocatalytic process can either directly participate in photocatalysis or produce ROS species ($^{\bullet}OH$, $^{\bullet}O_2^-$) that react with pollutants for photocatalytic decomposition into CO_2, H_2O and non-toxic products. Regulation and enrichment of photonic energy have a substantial effect in solar-assisted photocatalytic processes to enhance semiconductors' photocatalytic efficacy [11, 20-22].

Several discovered wide band gap photocatalysts have absorption in the ultraviolet (UV) region, while visible light active photocatalysts have a high recombination rate that limits their photocatalytic ability [23-27]. Other than these, limited light absorption range, the fast recombination rate of photocarriers, cost-effectiveness, time-consuming synthesis routes, and low permanency are the several challenges that impose hurdles during the practical application of photocatalysts [28-30]. Most photocatalytic nanomaterials are UV or partial visible light active photocatalysts and exhibit low solar-energy utilization. These photocatalysts are devoid of near-infrared (NIR) light absorption, thus, creating impediments in the progressive photocatalysis research [31, 32]. From this time, the invention and fabrication of NIR driven photocatalysts are highly needed as it contains ~52% (700 ~ 2500 nm) portion of the solar spectrum compared to ~5% (200 ~ 400 nm) and ~43% (400 ~ 700 nm) of UV, visible light, respectively [28, 33-35]. Numerous semiconducting nanomaterials (TiO_2, ZnO, g-C_3N_4, CuO) have been widely used in photocatalysis due to their high efficacy, nontoxicity, and photostability [36-38]. Still, the search for suitable photocatalysts has turned into a noble mission for researchers.

Among all these photocatalysts, graphitic carbon nitride (g-C_3N_4) has constricted energy gap (2.7 eV) and apt band potentials [12, 39, 40]. It is a metal-free, π-conjugated 2D nanomaterial with unique properties such as earth abundance, chemical inertness, good quantum yield, biocompatibility, firm luminescence, visible light harnessing, chemical and thermal stability that make it an efficient photocatalyst for photocatalytic processes [41-43]. Besides many unique possessions, charge carriers recombination, low surface area, and poor visible light absorption are the obstacles that hinder its photocatalytic ability for pollutant degradation and energy conversion [44, 45]. Therefore, many strategies, including structural amendments, reduction in thickness of g-C_3N_4 nanosheets *via* various thermal, mechanical, or liquid exfoliation treatments, doping, heterojunction formation, and coupling with support nanomaterials are the commonly used techniques to augment surface-active locates, prolong visible-light absorption toward longer wavelengths and to boost photoinduced charge carriers departure efficacy [46-49]. Other than these, extended light absorption towards the NIR region is a new and proficient way to uplift the photocatalytic ability of g-C_3N_4 [28, 29, 50].

Owing to low visible light absorption (~470 nm), g-C_3N_4 can only absorb blue light comprising a very slight amount of solar spectrum, which leads to inaccessibility of extended visible and IR light [51]. Henceforth, for efficient visible-NIR light utilization, modification in nanocomposites can be done through band gap engineering, coupling with noble metals (plasmonic effect) and carbon quantum dots, use of photosensitizer, heterojunction formation with narrow bandgap semiconductors, and upconversion (UC) [28]. To date, different noble metals and many accessible NIR dyes have been used in NIR photocatalysis, but due to high cost and thermal or other instability problems, they are not efficient [32]. Among all, the use of upconversion nanoparticles (UC NPs) has captured the interest of researchers due to their non-toxic, eco-friendly, and inexpensive (compared to other noble metals) nature [52]. When combined with UV-visible driven photocatalysts, they show NIR photons harnessing, which results in UV-visible light emission [32, 53, 54]. Radiant nanomaterials, *i.e.* lanthanide-ions-doped UC NPs can effectively transform lower photonic energy into higher photonic energy [55, 56]. These emissions are responsible for the excitation of other semiconductors (g-C_3N_4) and facilitate the indirect utilization of NIR photons during photocatalytic processes. Triplet-Triplet Annihilation is another method that can be used to attain UCL emission [57].

Many research reports have been published on g-C_3N_4 based heterojunction nanocomposite exhibiting UC properties for enhanced photocatalytic performance in waste water treatment and energy conversion *via* full solar light absorption (visible to NIR) [28]. The integration of Ln^{3+} UC NPs with $g\text{-}C_3N_4$ or $g\text{-}C_3N_4$ based nanocomposite to form a single photocatalyst and heterostructure is of great forthcoming in full solar light harnessing and for effective photocatalysis. In this review, we have discussed different types of lanthanides (Ln) and CQDs as UC nanomaterials to extend light absorption capacity. The present review also summarized the application of $g\text{-}C_3N_4$ based UC nanomaterials (lanthanides/Ln^{3+} and CQDs) in H_2 production and pollutant degradation via NIR light absorption. Similarly, various previously published reports have been discussed their photocatalytic mechanism.

2. Strategies responsible for inducing UC properties in photocatalysts to extend absorption in the NIR region

To attain efficient photocatalytic processes, one of the alluring and interesting practical strategies is the mingling of photocatalytic semiconducting nanomaterials with UC NPs [58]. To harvest the full solar spectrum, including NIR light, to upgrade the consumption of solar energy, and to improve photocatalytic reactions, UC is considered an effective method in photocatalysis [59]. UC is a nonlinear photosensitive approach that is generally used to convert low NIR photonic energy (two or multi) into a higher radiated photonic energy with a smaller wavelength covering UV to visible regions through the anti-Stokes luminescence method in photoexciting semiconductors [30, 55, 56]. The emitted photonic energy was then absorbed by UV-visible light-absorbing photocatalytic nanomaterials to indirectly utilize NIR light for photocatalysis. Due to the prolonged light harnessing power, NIR responsive nanomaterials possessing UC properties have gained a lot of interest [60]. In this regard, lanthanides ions (Ln^{3+}) and carbon-based quantum dots (CQDs) UC NPs have been employed to harvest a maximum portion of solar light during the photocatalytic process [28]. The amendment in size, components, and dopant amount of Ln and CQDs are the ways to up-convert light in UV to the visible wavelength. UC emission in photocatalysis can also be attained by Ln-based nanomaterials and through a triplet sensitized process.

2.1. Lanthanides (Ln) as UC NPs

Thus far, UC strategy has been extensively explored in numerous nanoscale host mediums, *e.g.* fluorides, oxides, vanadates, halides (chlorides, bromides, and iodides), oxysulfides, phosphates [61], etc. Generally, doping of Lanthanides ions (Ln^{3+}) in UC nanomaterials exhibits plentiful f-orbital configurations which show emission of narrow fluorescence bands due to intra-4f ($4f^n$-$4f^n$) or 4f-5d ($4f^n$-$4f^{n-1}5d$) orbitals transitions [59, 62]. Lanthanides are the major UC nanomaterials to achieve efficient spectral conversion due to their opulent energy level configuration (distinctive 4f electronic configuration in rare-earth elements) which permits facile photon arrangement [63]. During NIR light exposure, generated photons in the GS (ground state) of sensitizer got excited to ES (excited state) of activator/annihilators ions resulting in non-radiative or radiative relaxation of the population to activator ions of GS to attain UC emission. Outermost 5s and 5p shells of Ln^{3+} ions have a shielding effect which prevents nearby environmental consequences on electronic transitions [30]. This provides physicochemical stability against photobleaching and photodegradation. The effect of Ln^{3+} ions doped UC nanomaterials is generally represented by broad light absorption through the conversion of absorbed NIR light photons into visible light, as represented in Figure 1. The major absorption peaks situated at 808, 980, 1160 and 1530 nm are due to different Ln^{3+} ions *e.g.* Ho^{3+} ($^5I_8 \rightarrow {}^5I_6$) Nd^{3+} ($^4I_{9/2} \rightarrow {}^4F_{5/2}$), Er^{3+} ($^4I_{15/2} \rightarrow {}^4I_{13/2}$), Yb^{3+} ($^2F_{7/2} \rightarrow {}^2F_{5/2}$), correspondingly [64]. The incorporation of all these ions (Ln^{3+} ions) caused UC emissions as they behave as sensitizers and absorb focused NIR light resulting in UV or visible light photons emission *via* the energy transfer (ET) process [65]. Other than UCL emission of Ln^{3+} ions (such as Er^{3+}, Ho^{3+}, and Tm^{3+}), triplet-triplet activator-based UC is another way in which triplet states of a molecule (chromophores) generate intermediary excitation states [61]. The UC emission luminescence methods depend on rich f-electron conformations of Ln^{3+} ions. The conversion efficacy and emission spectra of Ln^{3+} ions doped nanomaterials are usually influenced by the inorganic host environment ($NaYF_4$, $NaGdF_4$, and CaF_2) and dopants (Yb/Ho, Yb/Er, Yb/Tm) compositional arrangements [33].

2.1.1. General mechanism of Ln UC nanomaterials

Generally, the UC mechanism is categorized into five different trails such as (i) excited state absorption, (ii) energy transfer upconversion (ETU), including successive energy transfer (SET), (iii) cross-relaxation (CR), cooperative upconversion (CU), and (v) phonon avalanche (PA) (Figure 1(a-f) [66, 67]. Out of all these methods, the ETU process is the best and most proficient UC pathway due to the presence of two different types of highly concentrated ions (donor as well as acceptor) in the near vicinity *via* dipole-dipole contact [52]. The amalgamation of Ln^{3+} ions with the photocatalyst/semiconductor can be done by either direct doping or by heterostructure formation. Typical xenon or halogen lamps, continuous-wave (CW) lasers, and fixated solar light can be used as light sources for the UC process. The common principle of the UCL procedure is explained in Figure 1 differentiating

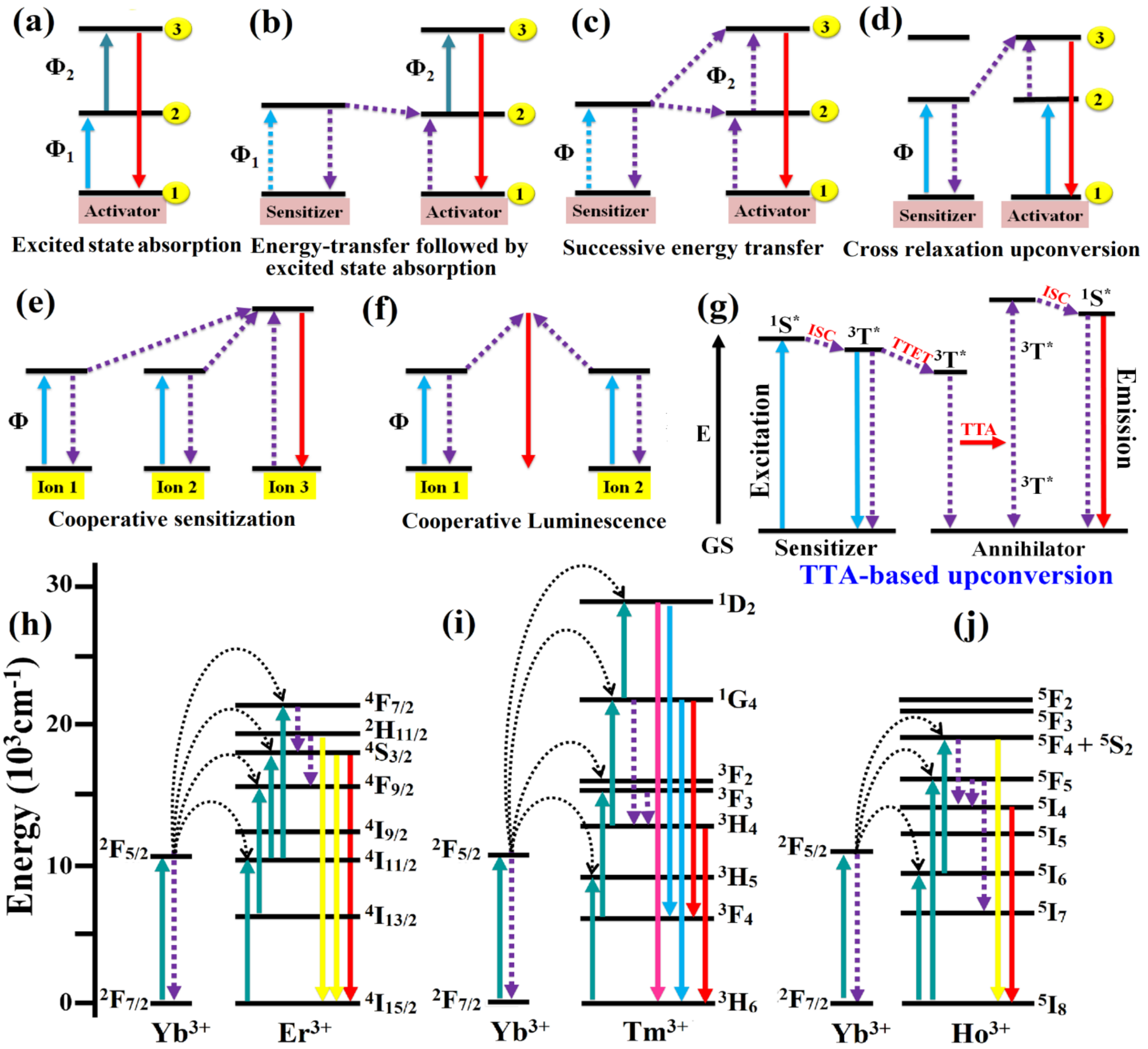

Figure 1. Diagrammatic representation of **(a)** Excited-State Absorption Process; **(b-f)** Energy-Transfer Up-conversion (ETU) Processes; **(b)** Energy-Transfer Followed by Excited-State Absorption, **(c)** Successive Energy-Transfers, **(d)** Cross-Relaxation UC, **(e)** Cooperative Sensitization and **(f)** Cooperative Luminescence. **(g)** General Energy-level diagram showing UC Process based on Triplet-Triplet Annihilation among Triplet State of Sensitizer and Triplet Annihilator. UC process of Lanthanide UC NPs Co-doped with **(h)** Yb^{3+} and Er^{3+}, **(i)** Yb^{3+} and Tm^{3+} and **(j)** Yb^{3+} and Ho^{3+}, Reprinted with permission from American Chemical Society (Copyright©2015) [61].

with the conventional PL process [61]. The process displayed absorption of energy from any excited photon or equivalent ET process in GS (1) of the luminescent center to attain ES (2). Afterwards, excitation of the luminescent center in the ES due to energy absorption from an additional photon or a resultant ET process (3). Then, reverse radiative transition occurs from ES (3) to GS or other lower-energy levels leading to the emission of a higher-energy photon. A metastable intermediate ES is achieved during the UCL system, which is divergent from the two-photon process and has a comparatively long lifespan to sustain a high populace in IES before another excitation energy.

2.1.2. Different types of Ln UC nanomaterials

UC process requires perfect host nanomaterials having low photonic energies to reduce non-radiative harm and make the best use of emission radiation. Halides (chlorides, bromides, and iodides) as host nanomaterials usually exhibit low photon energies (< 300 cm^{-1}) and due to their hygroscopic nature, they have restricted use [61]. Oxides as host materials possess high chemical stability and high photonic energy (> 500 cm^{-1}) [68]. Similarly, other frequently used host materials; fluorides have high chemical stability and low photonic energies (~500 cm^{-1}) [69]. Up to the present time, $NaYF_4$ is the most used host material for Ln UC NPs, and Er^{3+}, Tm^{3+}, and Ho^{3+} nanomaterials having ladder-like organized energy levels are the commonly used dopants. These dopants have been widely used as annihilators/activators to produce UC emission beneath CW lasers excitation. A comparatively < 2 mol % (minimal) amount of annihilators is used to reduce energy loss during cross-relaxation. All the activators' basic energy transfer mechanism is shown in Figure 1 [61]. As Figure 1g revealed, Yb^{3+} has a higher light absorption view than other Ln^{3+} activators, and the $^2F_{7/2} \rightarrow {}^2F_{5/2}$ transition of Yb^{3+} is suitably similar with many f-f transitions of Er^{3+}, Tm^{3+}, and Ho^{3+} resulting in effective ET from Yb^{3+} to other ions. Therefore, Yb^{3+} as a sensitizer is repeatedly co-doped with Er^{3+}, Tm^{3+} and Ho^{3+} to upgrade UC emission beneath 980 nm CW laser illumination (excitation source to counterpart the $^2F_{7/2} \rightarrow {}^2F_{5/2}$ transition of Yb^{3+}) [67, 70, 71]. The different ET process for Yb^{3+}/Er^{3+} co-doped UC NPs, Yb^{3+}/Tm^{3+} co-doped UC NPs and Yb^{3+}/Ho^{3+} co-doped UC NPs are shown in Figure 1 [61].

Among all host materials, fluoride nanocrystals (NCs) have been considered one of the good UC mediums. Due to intra 4f transitions, distinct optical possessions caused higher UC efficacy in rare-earth ions (RE^{3+}) doped $NaYF_4$ nanomaterials [72, 73]. Particularly, β-$NaYF_4$:Yb, Er/Tm NCs are exemplified as one of the greatest NIR-to-visible UC nanomaterials [74]. These were utilized as inter-medium for the transference of energy to g-C_3N_4 via NIR light absorption and resulted in strong photocarriers. The produced charge carriers then react with OH^-, H_2O and O_2 in the reaction mixture to generate different ROS (powerful non-selective oxidizing species) for energy conversion and to degrade pollutants. The development of NIR responsive g-C_3N_4/Ln based heterostructure nanomaterials has achieved a huge consideration in NIR-driven photocatalysis [28]. To explore the photocatalytic ability of g-C_3N_4/Ln heterostructure, Xu *et al.* synthesized Er^{3+} doped g-C_3N_4 photocatalyst exhibiting UC possessions by direct thermal polycondensation of $ErCl_3 \cdot 6H_2O$ + cyanuric acid-melamine (supramolecular material) [75]. The Er^{3+} doped g-C_3N_4 UC photocatalyst was then utilized for the removal of Rhodamine B (RhB) in the presence of visible light. In this work, the involvement of the Er^{3+} UC agent in the photocatalysis process was analyzed under red laser light (640−660 nm). The synthesized 2% Er^{3+} doped g-C_3N_4 nanocomposite exhibited increased degradation efficacy compared to bare g-C_3N_4 and displayed 100% removal of RhB dye within 40 min of light irradiation. Incorporation of Er^{3+} dopant in g-C_3N_4 augmented photoactivity by modifying electrochemical properties of g-C_3N_4. Additionally, photoactivity of Er^{3+} doped g-C_3N_4 nanocomposite was examined for H_2 generation under light exposure. The observed H_2 production rate of Er^{3+} doped g-C_3N_4 was higher (87 μmol h^{-1} g^{-1}) than bare g-C_3N_4 (80.2 μmol h^{-1} g^{-1}). exhibited higher rates than the pristine sample under white light Er^{3+} also minimized emission intensity and lifespan, which resulted in the generation of new, non-radiative deactivation paths. The plausible photocatalytic mechanism of Er^{3+}-doped g-C_3N_4 for RhB degradation was shown in Figure 2a presenting ET from Er^{3+} to g-C_3N_4 and localized energy levels in g-C_3N_4 generated by Er^{3+} dopant. Another research report on NIR responsive β-$NaYF_4$:Yb^{3+},Tm^{3+}/g-C_3N_4 (NYT/g-C_3N_4) photocatalytic material was given by Huang and coworkers for the elimination of colorless phenol and methyl blue (MB) [60]. The morphological results of NYT/g-C_3N_4 nanocomposite verified uniform deposition of hexagonal type $NaYF_4$ NCs (~20 nm diameter) on g-C_3N_4 NSs. The optical results represented NIR light absorption and transference of energy from NYT to g-C_3N_4. Photodegradation experiments confirmed higher photodegradation efficacy of NYT/g-C_3N_4 nanocomposite against MB and colorless phenol beneath 980 nm laser light exposure. The energy transfer mechanism of NIR responsive NYT/g-C_3N_4 nanocomposite was shown in Figure 2b. As shown in the mechanism, Yb^{3+} ions in GS $^2F_{7/2}$ were excited under NIR light (980 nm laser) and transferred to ES $^2F_{5/2}$ generating three consecutive ET processes from Yb^{3+} to Tm^{3+} which initiated colonizing of $^3H_5$, $^3F_2$, and $^1G_4$ levels. Consequently, non-radiative relaxation of $^3H_5$ and $^3F_2$ levels of Tm^{3+} took place to $^3F_4$ and $^3H_4$ levels, individually. But, because of large energy disparity (among the $^1G_4$ and $^1D_2$ levels), $^1G_4$ level of Tm^{3+} did not relax non-radiatively. The cross-relaxation amongst Tm^{3+} ions was accountable for $^1D_2$ level populations. It was excited to $^3P_2$ state *via* another ET from the excited $Yb^{3+,}$ which further relaxed non-radiatively to $^1I_6$ level. Excited Tm^{3+} ions fell to lower energy levels *i.e.* $^1I_6 \rightarrow {}^3F_4$, $^3F_3 \rightarrow {}^3H_6$, $^1D_2 \rightarrow {}^3H_6$, $^1G_4 \rightarrow {}^3H_6$, $^1D_2 \rightarrow {}^3F_4$ and $^1G_4 \rightarrow {}^3F_4$ at 345, 3 61, 451, 475, 646, 696 nm, respectively. Upon exposure to upconverted UV-visible light emissions, photoinduced charge carriers were produced in NYT/g-$C_3N_{4,}$ which formed highly reactive species ($^{\bullet}O_2^-$ and $^{\bullet}OH$) for the degradation of targeted pollutant. Similarly, core-shell nanostructured $NaYF_4$: Yb,Er/g-C_3N_4 ($NaYF_4$/CN) ternary composite was synthesized by Yang *et al.* using a simple two-step method [76]. During the synthesis process firstly, a hot cyanuric acid and a melamine solution were mixed followed by the addition of $NaYF_4$:Yb,Er to form a colloidal solution which resulted in ternary $NaYF_4$:Yb,Er-cyanuric acid-melamine adduct formation. The resultant adduct was then calcined at 550 ^oC, and $NaYF_4$/CN was attained as a final product. The $NaYF_4$/CN represented long-lasting UCL properties (Figure 2c) than bare $NaYF_4$:Yb,Er cubic NPs. The UC process displayed excitation of $NaYF_4$/CN photocatalyst under low energy photons (980 nm excitation), in which firstly, electrons of Yb^{3+} ions were excited and then get back to GS (relaxation process) either via irradiation or by transferring energy to Er^{3+} ions. This energy in Er^{3+} ions further caused excitation of the electron by other multiphoton processes and three emission peaks perceived at 655, 541, and 525 nm were assigned to $^4F_{9/2} \rightarrow {}^4I_{15/2}$, $^4S_{3/2} \rightarrow {}^4I_{15/2,}$ and $^2H_{11/2} \rightarrow {}^4I_{15/2}$ transitions in Er^{3+} ions, correspondingly. Another upconverted CeF_3/g-C_3N_4 nanoheterojunction was fabricated by Lu and his research group. The cerium fluoride (CeF_3) semiconductor having UC property was anchored on g-C_3N_4 NSs through microwave hydrothermal method [77]. The fabricated CeF_3/g-C_3N_4 nanocomposite with 40 wt% loading of CeF_3 revealed a higher photocatalytic desulfurization rate (84.2% within 3 h) compared to other synthesized photocatalysts. CeF_3 NPs exhibit superb UCL property which converted long-wavelength (Vis-NIR i.e. $\lambda > 460$ nm) light into UV light. The surface area of 40 wt% CeF_3/g-C_3N_4 nanocomposite was analyzed through N_2 adsorption-desorption isotherms which displayed type-IV distinctive hysteresis loop revealing mesoporous nature of nanocomposite. The porous nature of nanocomposite was helpful for the adsorption of DBT molecules. The observed BET specific surface area of pristine g-C_3N_4 and 40 wt% CeF_3/g-C_3N_4 was approx. 18.49 and 62.07 m^2/g signifying that incorporation of CeF_3 NPs on g-C_3N_4 surface efficiently enhanced surface area of nanomaterial. The general UC photodegradation process/mechanism of synthesized CeF_3/g-C_3N_4 nanocomposite was shown in Figure 2d beneath visible-NIR light illumination (420-460 nm). Additionally, both CeF_3 and g-C_3N_4 have well-aligned type-II heterostructures that promote photocarriers departure efficacy and photocatalytic efficiency of CeF_3/g-C_3N_4 towards dibenzothiophene (DBT). The photoexcited CB_{e-} of g-C_3N_4 migrated to CB of CeF_3 while VB_{h+} of CeF_3 moved towards VB of g-C_3N_4. The photoexcited e^- reacted with H_2O_2 to form $^{\bullet}OH$ radicals that oxidized DBT molecules into benzothiophene sulfone molecules further extracted and eliminated from model oil. However, photoinduced h^+ in VB unable to produce $^{\bullet}OH$ radicals due to insufficient VB potential.

2.2. Triplet-Triplet Annihilation (TTA) UC mechanism

Triplet-Triplet Annihilation (TTA) is a method that can be used to attain UCL emission [78]. Parker and co-workers first reported TTA process in the 1960s elucidating organic chromophores with absorption and emission properties in the

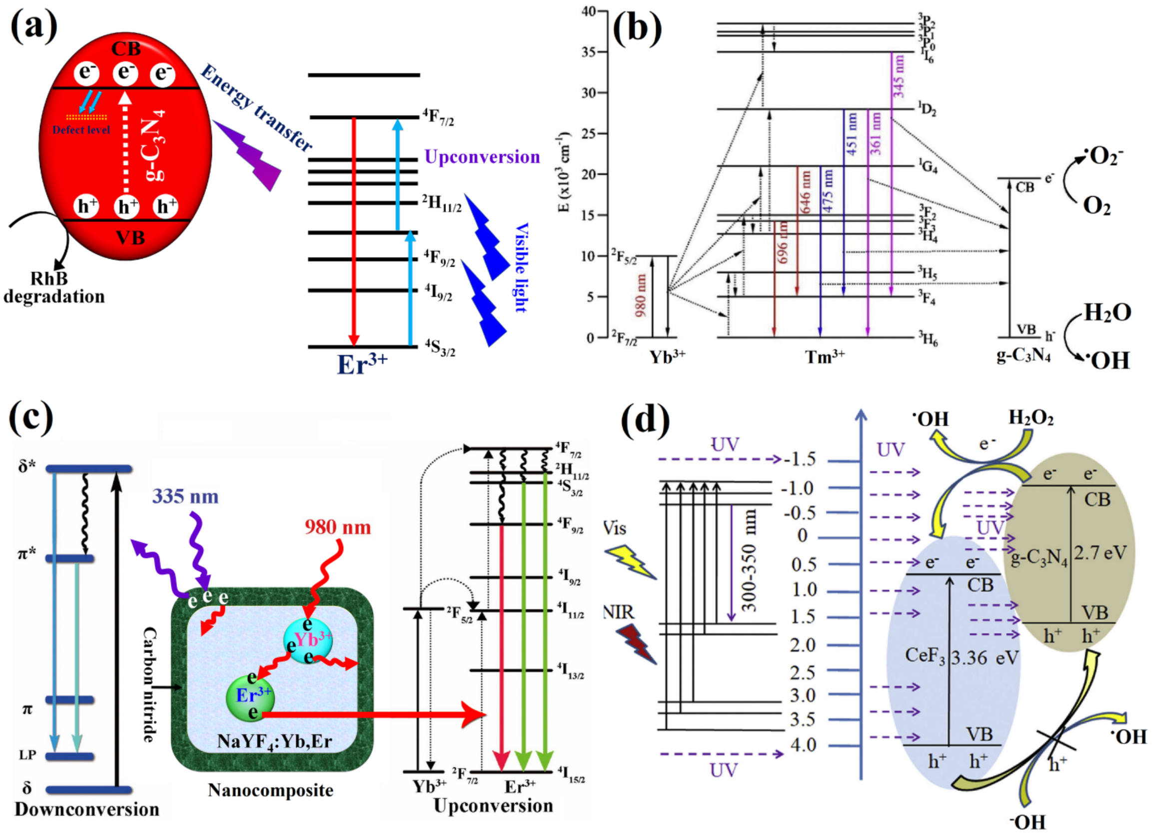

Figure 2. **(a)** Diagrammatic representation of RhB degradation mechanisms using Er^{3+}-doped $g-C_3N_4$, Reprinted with permission from American Chemical Society (Copyright©2014) [75]. **(b)** Graphic depiction of energy levels of Yb^{3+}-Tm^{3+} and energy transferal route from NYT to $g-C_3N_4$ beneath 980 nm laser light radiation, Reprinted with permission from Elsevier (License No. 5183110718712) [60]. **(c)** Schematic design of luminescence mechanism of $NaYF_4$/CN under 980 nm or 335 nm excitation wavelength, Reprinted with permission from Elsevier (License No. 5183110927652) [76]. **(d)** Proposed photodegradation process of CeF_3/$g-C_3N_4$ nanocomposite, Reprinted with permission from Elsevier (License No. 5183111437293) [77].

UV region [79]. TTA-based UCL emission can be perceived through an uncovered eye on excitations under green laser light at 532 nm (low power) [80]. Recently, some organic dyes and metal complexes exhibiting TTA-based UCL emission have been discovered, revealing a light spectral range from UV-NIR [57]. In TTA based UC process, sensitizers and annihilators are molecule-based chromophores with triplet states as IES. In this process, firstly, the sensitizer is photoexcited to its singlet ES 1S* *via* excitation of longer wavelength, which is then trailed by ISC (Intersystem crossing) to obtain triplet state 3T*. Afterwards, for the regeneration of GS in sensitizer, triplet-triplet energy transfer (TTET) occurs due to relocation of triplet energy from sensitizer to annihilator (Figure 1f). The former process happened repetitively to generate several long-lasting triplets annihilator, so that TTA process can take place proficiently. At the end, annihilator in ES comes back to GS by radiative transition route to result in UC emission. From time to time, annihilator is also named as emitter. Many reports on $g-C_3N_4$ based Triplet-Triplet Annihilation have been published revealing UC process for energy production and pollutant degradation. A highly efficient and comprehensive range photoresponse $g-C_3N_4$-CdS NSs based plasmonic (incorporation of Au NPs) TTA UC photocatalyst was reported by Fang and his research group for photocatalytic H_2 production [81]. To solve aggregation and photo corrosion problems as well as to enhance the stability, CdS was coupled with $g-C_3N_4$ to form $g-C_3N_4$-CdS nanocomposite heterojunctions, which were then further amalgamated with Au-PtDPA@

SiO_2 NPs. The results verified that g-C_3N_4-CdS NSs based Au-amended TTA-UC utilized upconverted higher-energy phonons and resulted in superior photocatalytic H_2 production, *i.e.* 16.88 µmol g^{-1} beneath visible-light illumination and 1.439% apparent quantum efficiency (AQE) rate under green-light illumination. The superior photoactivity was due to TTA-supported UC photocatalysis and Au plasmon resonance effect. Heterostructure formation of enhanced g-C_3N_4@CdS with Au-enhanced TTA-UC NPs was shown in Figure 3a. TTA-UC nanomaterials were excited by lower energy green light phonons of solar light and incorporation of Au NPs enhanced UC efficacy due to MPR augmented absorption of excitation light. Upon solar light illumination both of CdS and g-C_3N_4 photocatalysts produced photoinduced charge carriers and well aligned as well as overlapped band structure caused vice versa transference of charge carriers. The received h^+ by g-C_3N_4 participated in the oxidation of TEA while transferred e^- to the CB of CdS was transferred to Pt (noble metal) for the reduction of proton to form H_2. Due to apt energy gap alignment (heterostructure formation) and incremented higher-energy phonons from Au-amended TTA-UC, g-C_3N_4@CdS was sensitized efficaciously which resulted in enhanced photocarriers separations and H_2 production rate.

2.3. Carbon-based quantum dots (CQDs) as UC NPs

Another UC nanomaterial is carbon-based quantum dots comprising carbon nanodots (CNDs) and graphene quantum dots (GQDs) (size < 10 nm diameter). CQDs are green, copious, environmentally friendly, nontoxic, and recyclable carbon-based materials keeping stable size and excitation wavelength-dependent PL properties (due to quantum confinement effects) [82, 83]. On the other hand, effective photocarrier acceptance and transference are practical approaches that suppress the recombination rate of charge carriers. CQDs are harmless carbon NPs having various exceptional properties like detectible water-solubility, biocompatibility [84], promising electrical conductivity [85], reducibility [86], etc. Owing to these possessions, CQDs have various applications in different fields such as fluorescence or electrochemical measurements [87, 88], photo-photoelectrochemical catalysis [89, 90], and chemiluminescence nanomaterials [91], etc. In photocatalysis, CQDs not only act as an electric buffer to receive or to transfer electrons towards adjacent semiconductors but also exhibit concurrent down- and up-conversion PL possession that make it an excellent photosensitizer to capture visible and NIR light [84, 92]. Photoexcited conjugated π-electrons in sp^2 carbon complex and oxygen-comprising groups at the surface are responsible for UC possessions in CQDs [93]. Beneath NIR light illumination, CQDs display extensive UC emission in the range of UV to visible, while fluorescence emissions of CQDs are reliant on NIR wavelength, particle size dispersal, emissive traps of intrinsic defects, and surface functional groups [94, 95].

Additionally, different heteroatoms doping and other surface environments also affect the UC efficacy of CQDs and make UCL amendable [96]. Similarly, its unique structural properties provide photo-stability and facile-complexation of CQDs with other semiconducting materials and metallic NPs. Therefore, CQDs exhibiting up-and down-converted PL and photo-excited electron transferals capability contribute to strong NIR harnessing. In this favor, several g-C_3N_4/CQDs-based photocatalytic nanocomposites have been explored with their extraordinary photocatalytic degradation and H_2 production capabilities using a broad solar spectrum [28].

Based on previous data, CQDs were validated as electron acceptors and donors. Coupling of CQDs with ultrathin g-C_3N_4 nanosheets (UCN NSs) explored by Liu *et al.* elucidated enhanced light-harvesting possessions of g-C_3N_4 to the broader spectral range with improved charge carriers separation [97]. To prepare 2D/0D CQDs/UCN nanocomposite, CQDs were first synthesized through rapeseed flower bee pollens and then combined with UCN NSs (prepared from dicyandiamide) through hydrothermal route. The structural results verified uniform deposition of CQDs on UCN NSs linkage through stacking interactions. The characterization results revealed that CQDs served as an electron transferal intermediary to enhance photocarriers' departure and prolong their lifespan. The photocatalytic results displayed a higher H_2 production rate of UCN/CQDs-0.2% nanocomposite (88.1 µmol/h) which was 9.79, 3.02, and 1.91 times greater than bulk g-C_3N_4, bare UCN, and BCN/CQDs-0.2%,

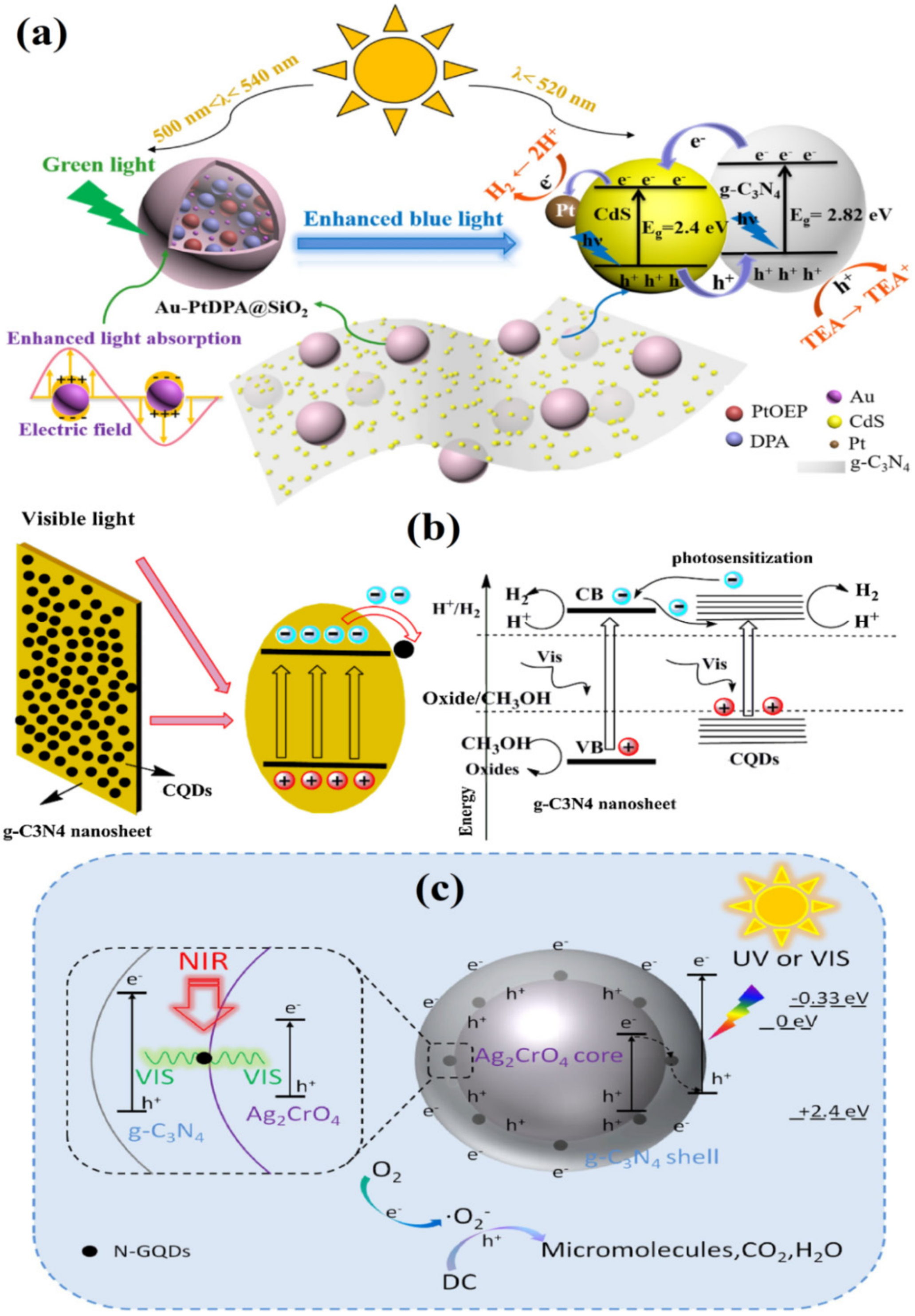

Figure 3. **(a)** Diagrammatic representation of the photocatalytic mechanism of g-C_3N_4@CdS nanocomposite centered on Au-enhanced TTA-UCL route [81]. **(b)** Schematic design of photodegradation process of UCN/CQDs nanocomposite beneath visible light exposure (> 420 nm) [97]. **(c)** Diagrammatic representation showing UC and photocatalytic charge transfer mechanism with photocorrosion inhibition for AN@CN nanocomposites [98], Reprinted with permission from Elsevier (License No. 5183170171682, 5183170337473, 5183170457870).

respectively. The proposed photocatalytic mechanism of CQDs/UCN nanocomposite is shown in Figure 3b. Initially, beneath visible light illumination, the photogenerated electrons of UCN were migrated to CQDs. Due to theelectron-accepting and conducting nature of CQDs, the free electrons in CQDs suppressed photocarriers recombination. Secondly, the π-conjugated structure of CQDs acted as photosensitizer (sensitization of UCN by organic dyes). It caused donation of e^- to $UCN_{CB,}$ which promoted visible light harvesting and enhanced photocatalytic H_2 generation rate. Finally, CQDs' upconversion photoluminescence (UC PL) properties lead to longer wavelength light absorption by emitting the shorter wavelength light. Likewise, Che *et al.* reported N-doped graphene quantum dots (NGQDs) amended Z-scheme g-C_3N_4/Bi_2WO_6 (NGQDs/g-C_3N_4/Bi_2WO_6) nanoheterojunctions exhibiting entire light adsorption property and enhanced photocarriers departure efficiency [99]. NCQDs were fabricated through the hydrothermal method and infatuated with numerous active sites in this work. The photoactivity of prepared photocatalysts was examined against tetracycline (TC), ciprofloxacin (CIP), and oxytetracycline (OTC) with the assistance of visible and NIR light exposure. The highest photodegradation ability was analyzed by NGQDs/g-C_3N_4/Bi_2WO_6 nanocomposite due to UCL properties and photocarriers capturing effect (electron sink behavior) of NGQDs boosted photocarriers separation efficacy. In previous research work, it was also proved that CQDs acted as photosensitizers in CdS/CQDs/g-C_3N_4 nanocomposite to efficiently absorb full solar spectrum and enhance photodegradation ability. Other results on GQDs were published by Feng *et al.* by synthesizing core-shell N-GQDs/ Ag_2CrO_4@g-C_3N_4 nanocomposites having anti-photo corrosion ability and upgraded full solar spectrum light absorption [98]. Optical results validated the light absorption of prepared Ag_2CrO_4 and g-C_3N_4 photocatalysts in UV and visible light, while N-GQDs absorbed NIR light and significantly enhanced full solar light harnessing. Furthermore, the excellent conductive nature of N-GQDs and core-shell organization (incremented contact area among Ag_2CrO_4 and g-C_3N_4) promoted photocarriers transmission ability from Ag_2CrO_4 to g-C_3N_4 efficiently and not only suppressed their recombination rate but also inhibited photocorrosion of Ag_2CrO_4. The researcher have analyzed photodegradation efficacy of all synthesized photocatalysts against doxycycline beneath full solar spectrum light. The proposed Z-scheme mechanism of nanocomposite was shown in Figure 3c representing generation of photocarriers in g-C_3N_4 and Ag_2CrO_4 beneath the exposure of UV-visible light which further produced ROS. The presence of N-GQDs had successfully absorbed NIR light and resulted in emission of visible light (425-520 nm) *via* two-photon UC PL procedure. Similarly, it has also enhanced Z-scheme electron migration pathway and improved photocarriers separation efficiency. The photocatalytic mechanism explained a crucial part of $^{\bullet}O_2^-$ radicals and h^+ in doxycycline degradation.

3. Photocatalytic applications of NIR-responsive upconverted g-C_3N_4 based nanomaterials

UC responsive photocatalytic nanomaterials mainly exhibit light absorption afar from the UV-visible region and catalyze photocatalytic reactions via accumulated upconverted photon energy, i.e. NIR to UV-visible [54]. Nowadays, UC active photocatalysts have gathered a lot of interest for renewable energy conversion (H_2 production) and waste water treatment. The next section has a detailed discussion on g-C_3N_4 based UC nanomaterials (Lanthanides/ Ln^{3+} and CQDs) for H_2 production and pollutant degradation.

3.1. g-C_3N_4 based UC nanomaterials for H_2 production

3.1.1. Ln doped UC NPs/g-C_3N_4 nanomaterials

Lanthanide-doped UC nanomaterials mainly comprise a host matrix which is an inorganic crystalline ($NaYF_4$) and trivalent lanthanide ions (Ln^{3+} ions) that act as sensitizers (Yb^{3+}) and activators (Er^{3+} and Tm^{3+}), imbedded in the host lattice [52, 61]. Many reports were published on NIR light-assisted photocatalytic hydrogen production using upconverted g-C_3N_4 based nanomaterials and some of them have been discussed ahead. For example, Zhu and his peer group synthesized C_3N_4 nanotubes-based nanomaterials heterostructure employing a facile chemical technique for NIR-assisted photocatalytic H_2 production [58]. In this work, UC NPs, i.e. $NaYF_4$:Yb,Tm (NYF), $NaYF_4$:Yb,Tm,Gd (NYFG), and C_3N_4 nanotubes (C_3N_4 NTs) were fabricated using solvothermal and calcination cum water-induced morphological transformation method, respectively. After that, prepared UC NPs were adorned on C_3N_4 NTs independently to form nanoheterojunctions. The photocatalytic results revealed that NYFG/C_3N_4 NTs having 15% loading amount of UC NPs had higher (311.6 μmol g^{-1}) H_2 production rate which was approx. 1.4 times greater than NYF/C_3N_4 NT nanoheterostructure beneath 980 nm laser light exposure and 0.80‰ AQE value. Furthermore, all-inclusive results verified augmented photocatalytic proficiency of Gd doped nanoheterostructure due to synergic effect, resilient interaction, and higher emission intensities. The increased photocarriers transferal efficacy of UC NPs/C_3N_4 NTs nanocomposite was confirmed through PL analysis which was ascribed to strong interaction among UC NPs and C_3N_4 NTs. Similarly, an illustrative schematic representation of energy transmission and reaction mechanism in NYFG(15)/C3N4 NTs nanocomposite was explored to validate the NIR-driven photocatalytic ability. Excitation of only Yb^{3+} ions was observed beneath NIR light illumination when impelling 980 nm light which acted as a sensitizer and resulted in the generation of three consecutive energy transferences from Yb^{3+} to Tm^{3+} ions due to $^3H_5$, $^3F_{2,3,}$ and $^1G_4$ energy levels colonizing. Similarly, a cross-relaxation course among Tm^{3+} ions was accountable for colonizing $^1D_2$ level, and Gd^{3+} ions could not absorb 980 nm photons straightly. But, in Yb^{3+}-Tm^{3+}-Gd^{3+} tridoped UC system, highly excited Tm^{3+} ions transferred energy to Gd^{3+} and boosted its excitation. Then C_3N_4 NTs directly get excitation after energy transference by highly excited levels of Tm^{3+} and Yb^{3+} ions *via* the F¨orster resonance energy transfer (FRET) route. Accordingly, charge carriers were generated in VB and CB of C_3N_4 NTs. The excited electrons reacted with water molecules to form H_2, while collected h^+ reacted with TEA to produce diethylamine (DEA) and acetaldehyde underneath NIR light exposure. The photocatalytic reactions verified extended light harnessing of prepared UC NPs based C_3N_4 NTs photocatalysts towards the NIR region.

Similarly, Zhao *et al.* prepared a unique UCNPs @SiO_2@Ag/g-C_3N_4 nanoheterostructure (UCNPs: $NaLuF_4$:Gd,Yb,Tm@$NaLuF_4$:Gd,Yb) to enhance solar light harnessing the ability of g-C_3N_4 for H_2 generation and RhB degradation [100]. UV-Vis-NIR DRS results disclosed an absorption band at around 980 nm in the NIR region, verifying extended solar light absorption due to incorporating UC NPs in UCNPs@SiO_2/g-C_3N_4 (Figure 4a). This observed absorption band was ascribed to $^2F_{7/2} \rightarrow {}^2F_{5/2}$ transition by Yb^{3+} ions in UC NPs (Yb^{3+} ions absorb light 980 nm and exhibit excitation owing to $^2F_{7/2} \rightarrow {}^2F_{5/2}$ transition) as shown in (Figure 4c). The characterization results displayed good solar light-harvesting capability and speedy charge carriers separation efficacy (confirmed through PL analysis) (Figure 4b). The photodegradation results verified a 10 and 12 times increase in RhB removal and H_2 evolution efficiency by UCNPs@SiO_2@Ag/g-C_3N_4 heterostructure than bare g-C_3N_4. The observed H_2 production rate of S1, S2, S3, and S4 were displayed in Figure 4d beneath 5 h of simulated sunlight irradiation. The tremendous photoactivity of nanocomposite was due to the combined effect of both UC NPs and Ag NPs (NPs) that augmented the photocatalytic ability of g-C_3N_4. The proposed photodegradation mechanism of UCNPs@SiO_2@Ag/g-C_3N_4 nanocomposite for RhB removal was explored and displayed in Figure 4e.

Additionally, work on H_2 generation was also described by Murali and coworkers by preparing a novel upconverted NIR driven Z-scheme $NaYF_4$:Yb/Tm@Ag_3PO_4/Ag@g-C_3N_4 nanocomposite (NYFT@AP/Ag@CN) [101]. The full solar spectrum responsive NYFT@AP/Ag@CN nanocomposite was fabricated using a simple synthetic route where Ag_3PO_4/Ag NPs and g-C_3N_4 NSs were successively deposited on $NaYF_4$:Yb/Tm UC hexagonal disks (Figure 5a). The morphological results of $NaYF_4$:Yb/Tm (NYFT), $NaYF_4$:Yb/Tm@Ag_3PO_4/Ag (NYFT@AP/Ag), and NYFT@AP/Ag@CN nanomaterials were shown in Figure 5(b-g). To analyze the light absorption properties of prepared photocatalysts, UV-Vis-NIR DRS studies have been explored, representing full sunlight absorption (UV-Vis-NIR) owing to UC NPs (Figure 6a). NYFT UC NPs caused coinciding UV-visible emissions *via* UC route under NIR light photons during solar light exposure. The absorption peaks of NYFT UC NPs perceived at 797, 690, 470, and 360 nm were due to $^3H_6 \rightarrow {}^3H_4$, $^3H_6 \rightarrow {}^3F_{2,3}$, $^3H_6 \rightarrow {}^1G_4$ and $^3H_6 \rightarrow {}^1D_2$ transitions of Tm^{3+} ions, correspondingly, however wide and strong absorption band observed at 976 nm was attributed to $^2F_{7/2} \rightarrow {}^2F_{5/2}$ transition of Yb^{3+} ion. Furthermore, in NYFT@AP/Ag nanocomposite, the absorption peak at

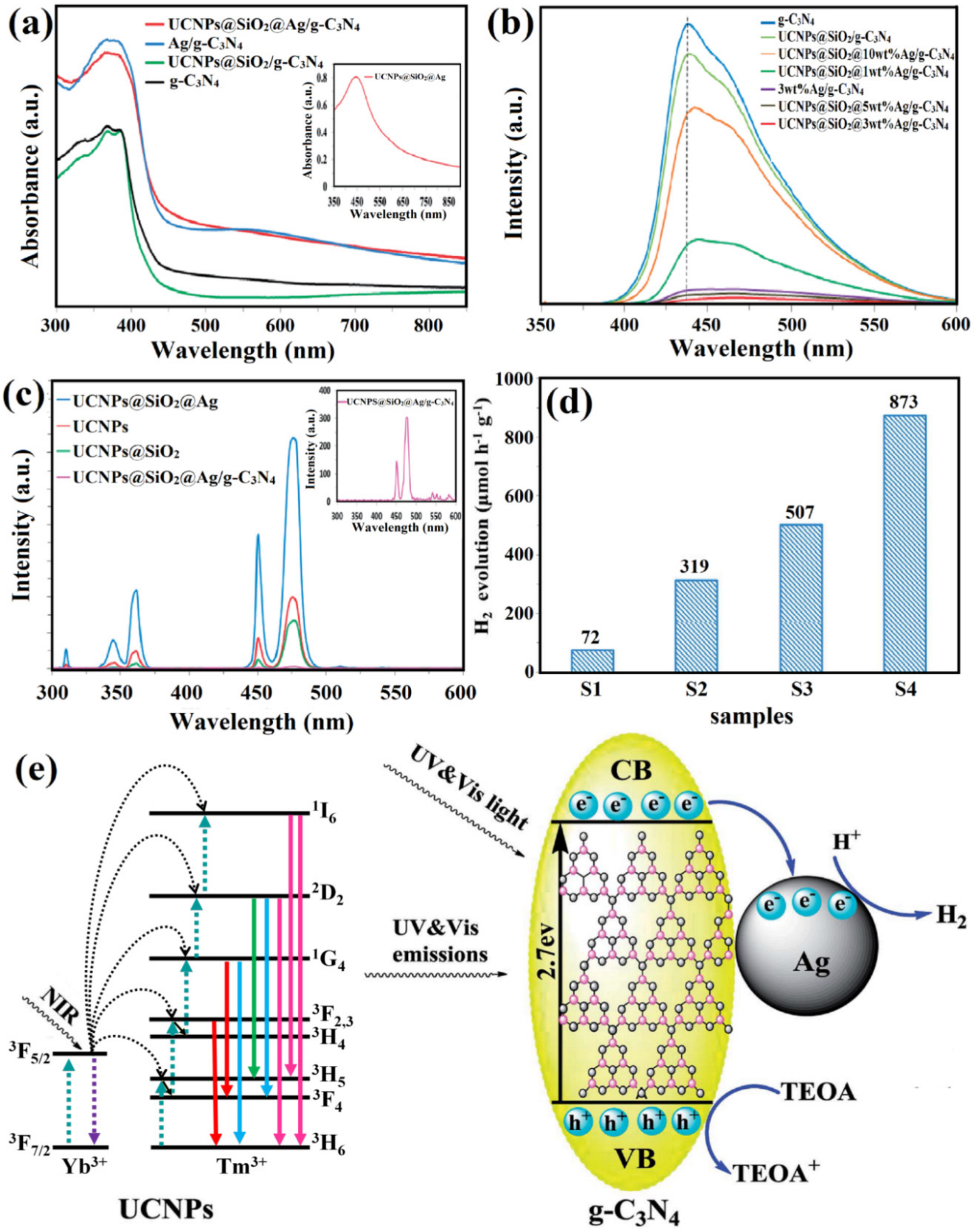

Figure 4. **(a)** UV-Vis-NIR DRS results of g-C_3N_4, UCNPs@SiO_2/g-C_3N_4, 3 wt% Ag/g-C_3N_4, and UCNPs@SiO_2@3wt%Ag/g-C_3N_4 photocatalysts (inset indicates the absorption spectrum of UCNPs@SiO_2@Ag in water), **(b)** PL and **(c)** UCL spectra (under 980 nm excitation) of different synthesized photocatalysts, **(d)** H_2 production rates of g-C_3N_4, UCNPs@SiO_2/g-C_3N_4, 3wt%Ag/g-C_3N_4 and UCNPs@SiO_2@3wt%Ag/g-C_3N_4 (S1, S2, S3, and S4) under 5 h of simulated sunlight irradiation and **(e)** Photodegradation mechanism of UCNPs@SiO_2@Ag/g-C_3N_4 nanocomposite under simulated sunlight exposure, Reprinted with permission from Royal Society of Chemistry (Open Access- Licensed under a Creative Commons Attribution-3.0) [100].

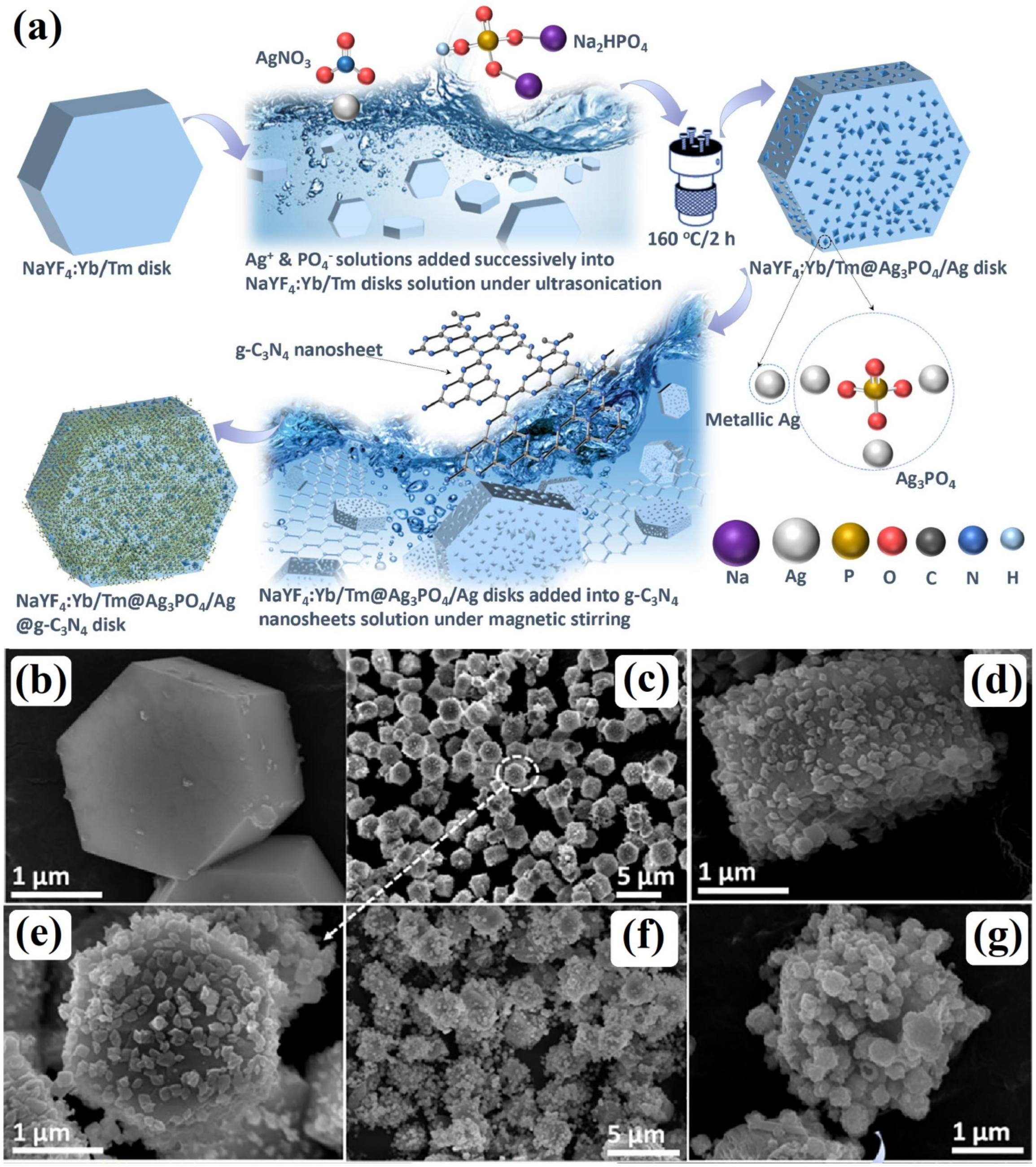

Figure 5. **(a)** Graphic representation of synthetic route of NaYF4:Yb/Tm@Ag3PO4/Ag@g-C3N4 nanocomposite and **(b-g)** FE-SEM micrographs of prepared **(a)** NaYF4:Yb/Tm, **(b-d)** NaYF4:Yb/Tm@Ag3PO4/Ag, and **(e, f)** NaYF4:Yb/Tm@Ag3PO4/Ag@g-C3N4 nanostructures, Reprinted with permission from Elsevier (License No. 5183170960425) [101].

525 nm has corresponded to Ag$_3$PO$_4$/Ag with absorption peaks of NYFT. Covering of g-C$_3$N$_4$ did not cause any notable changes in the absorption spectrum. The UC PL spectra of all prepared photocatalysts were presented in Figure 6b beneath 980 nm laser excitation. The emission peaks displayed at around 474, 450, 360, 344, and 288 nm were resembled $^1G_4 \rightarrow {}^3H_6$ $^1D_2 \rightarrow {}^3F_4$, $^1D_2 \rightarrow {}^3H_6$, $^1I_6 \rightarrow {}^3F_4$, and $^1I_6 \rightarrow {}^3H_6$ transitions of Tm^{3+} ions for NYFT disks, correspondingly. Light absorption by AP/Ag@CN shell permitted extra photons to increment photocarriers separation.

The existence of metallic Ag prevented a fast recombination rate in g-C_3N_4 due to the rapid migration of electrons from Ag_3PO_4 to Ag and Ag to g-C_3N_4. This facilitated the existence number of an excited e^- (having more reduction power) in g-C_3N_4 for H_2 generation. The NYFT@AP/Ag@CN nanocomposite exhibited a 23.56 μmol/g/h H_2 production rate that was 2.6 and 1.4 folds more than NYFT@AP/Ag (9.05 $\mu molg^{-1}h^{-1}$) and NYF@AP/Ag@CN (16.32 μmol/g/h) nanocomposite, correspondingly as shown in Figure 6c. The H_2 production rate of NYFT@AP/Ag@CN photocatalyst was also explored under UV, visible, NIR, and full sunlight illumination (Figure 6d). Based on DRS and UC studies, the proposed NIR-light assisted photocatalytic mechanism with energy transfer process has been illustrated in Figure 6e representing H_2 evolution. As shown in the mechanism, existing NIR photons excited Yb3+ ions in NaYF4 (2F7/2 → 2F5/2) due to solar light illumination, which further acted as sensitizers to colonize higher energy levels of Tm^{3+} ions. Subsequently, non-radiative relaxation of Tm^{3+} ions populated other energy levels, and their energy was transported directly to the AP/Ag@CN shell located in the $NaYF_4$:Yb/Tm core through the FRET procedure. This caused excessive charge carrier production where Ag^0 acted as a passage among Ag_3PO_4 and g-C_3N_4, promoting recombination of VB h^+ of g-C_3N_4 with CB e^- of Ag_3PO_4. Hence, the lifespan of g-C_3N_4 CB e^- and Ag_3PO_4 VB h^+ was enhanced, leading to the reaction of electrons with H_2O and holes with lactic acid to produce H_2 and pyruvic acid respectively. The whole mechanism followed a Z-scheme pathway, as shown in Figure 6e.

3.1.2. CQDs UC NPs/g-C_3N_4 nanomaterials

CQDs also show UC properties, and there are some reports on CQDs-based UC properties in hydrogen production and pollutant degradation [28]. Besides this, the coupling of UC CQDs with g-C_3N_4 has also been explored, showing a NIR-driven photocatalytic reaction. Some of the reports on UC CQDs/g-C_3N_4 nanocomposite have been discussed in this section. For instance, Wang *et al.* fabricated g-C_3N_4/quantum dots (CNQDs) nanocomposite using already synthesized bulk g-C_3N_4 and employing a thermal-chemical etching route [102]. The strong blue emission and UC properties were the main energy transmission route in synthesized visible light-responsive CNQDs based photocatalysis. PL spectra of synthesized nanomaterials displayed bright blue emission by CNQDs under UV excitation. A red shift in the peak was observed from 340-420 nm, and at 360 nm excitation wavelength, a high-intensity peak was perceived. The inherent PL properties of CNQDs were generally due to p-p* transition. Similarly, CNQDs displayed UC properties under longer wavelength light exposure (705 to 862 nm). Light emissions were generated at 350 to 600 nm wavelength have covered almost full visible region. Mainly, the multiphoton active method and anti-Stokes PL were responsible for UC emission and even the multiphoton active method was more apt to describe UC emission of CNQDs. Both PL and UC emission spectra confirmed NIR to the visible light conversion of CNQDs. Also, the observed H_2 production rate for bare g-C_3N_4 and CNQDs was 48.05 and 109.96 μmol h^{-1} (5 mL CNQD), and on further increasing CNQDs wt. to 10 mL, the H_2 production rate got boosted up to 137.84 μmol h^{-1}. Huang and his research group also synthesized 3D, and porous g-C_3N_4 quantum dots amended g-C_3N_4/GO NSs aerogel (CNGO/CNQDs) *via* hydrothermal and vacuum injection procedure for UV-Vis-NIR light assisted photocatalytic H_2 generation [103]. A schematic diagram of CNGO/CNQDs synthesis is shown in Figure 7a. In the distinctive ternary nanocomposite, GO (graphene oxide) acted as support nanomaterial and enhanced photocarriers migration and departure efficacy. However, the 3D web framework of aerogel's offered more active sites. Simultaneously, due to suitable UC possessions of CNQDs and CNGO/CNQDs, light harnessing was prolonged from UV to NIR which endowed enhanced photocatalytic ability to photocatalysts. UC luminescence spectra of CNQDs were displayed in Figure 7b with light excitation from 630 to 850 nm. The UC emission results of CNQDs were nearly surrounded by light absorption spectra of CN-5, resulting in upgraded absorption of the full solar spectrum (visible–NIR light) light. Fluorescence emission results of CNGO and CNGO/CNQDs photocatalysts at 725 nm excitation wavelength were presented in Figure 7c. UV-Vis DRS results verified stronger and broader light absorption by CNGO/CNQDs compared to CN-5 and CNGO owing to light absorption and multiple light scattering by GO and aerogel's porous structure (Figure 7d). The observed forbidden band gap of CN-5 was approx. 2.3 eV, calculated by Kubelka-Munk function (Inset of the figure). The attained H_2 production efficacy of CNGO/CNQDs

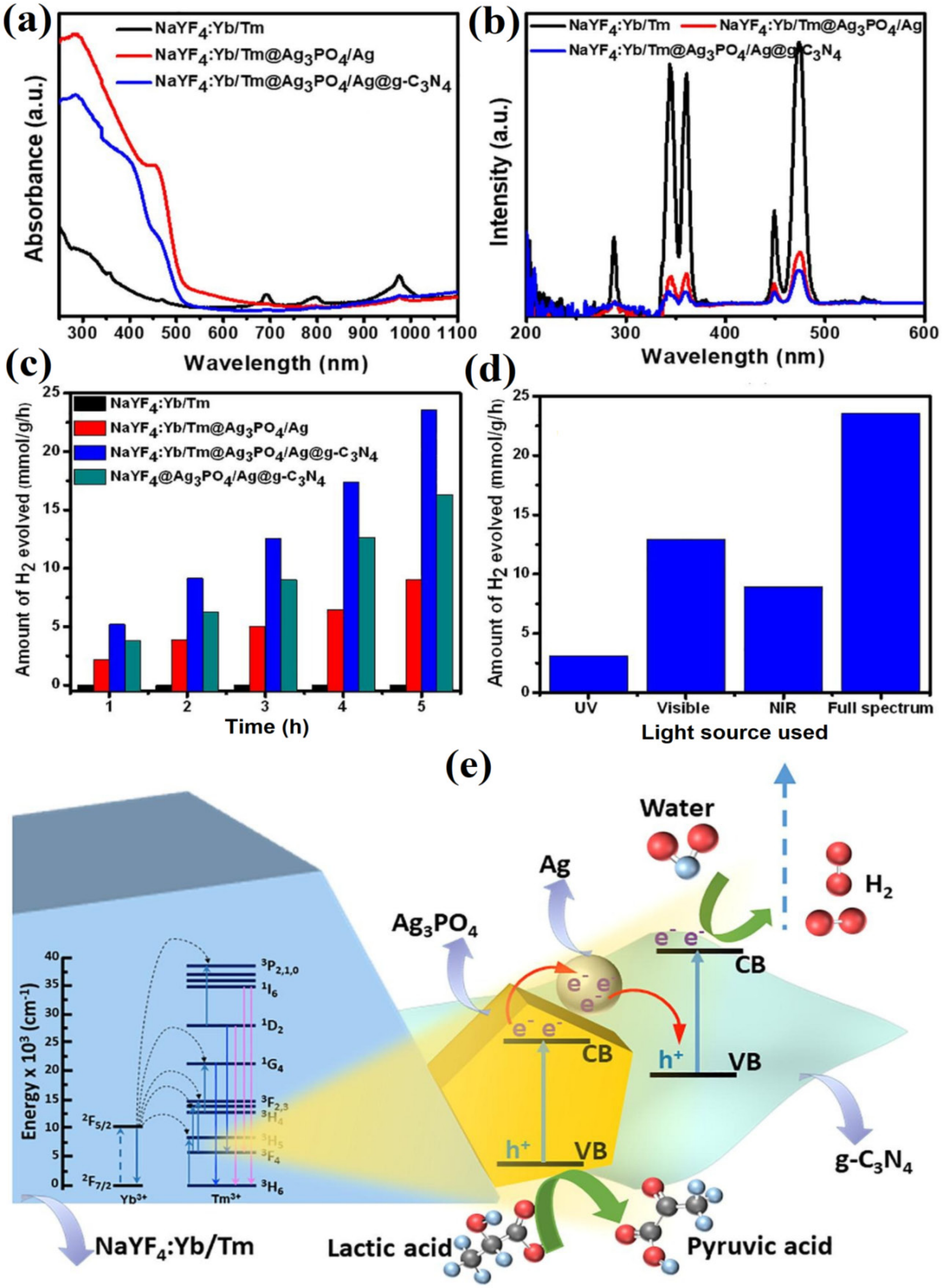

Figure 6. **(a)** Optical absorption and **(b)** UC PL spectra of as-prepared photocatalysts. **(c)** Evaluation of H_2 production rate of differently prepared photocatalysts in 10% lactic aqueous acid solution and **(d)** Hydrogen production rate by NYFT@Ag_3PO_4/Ag@g-C_3N_4 photocatalysts under UV-visible-NIR and full solar light illumination. **(e)** Diagrammatic depiction of the photocatalytic Hydrogen generation mechanism of NYFT@ Ag_3PO_4/Ag@g-C_3N_4 photocatalyst beneath solar light exposure, Reprinted with permission from Elsevier (License No. 5183170960425) [101].

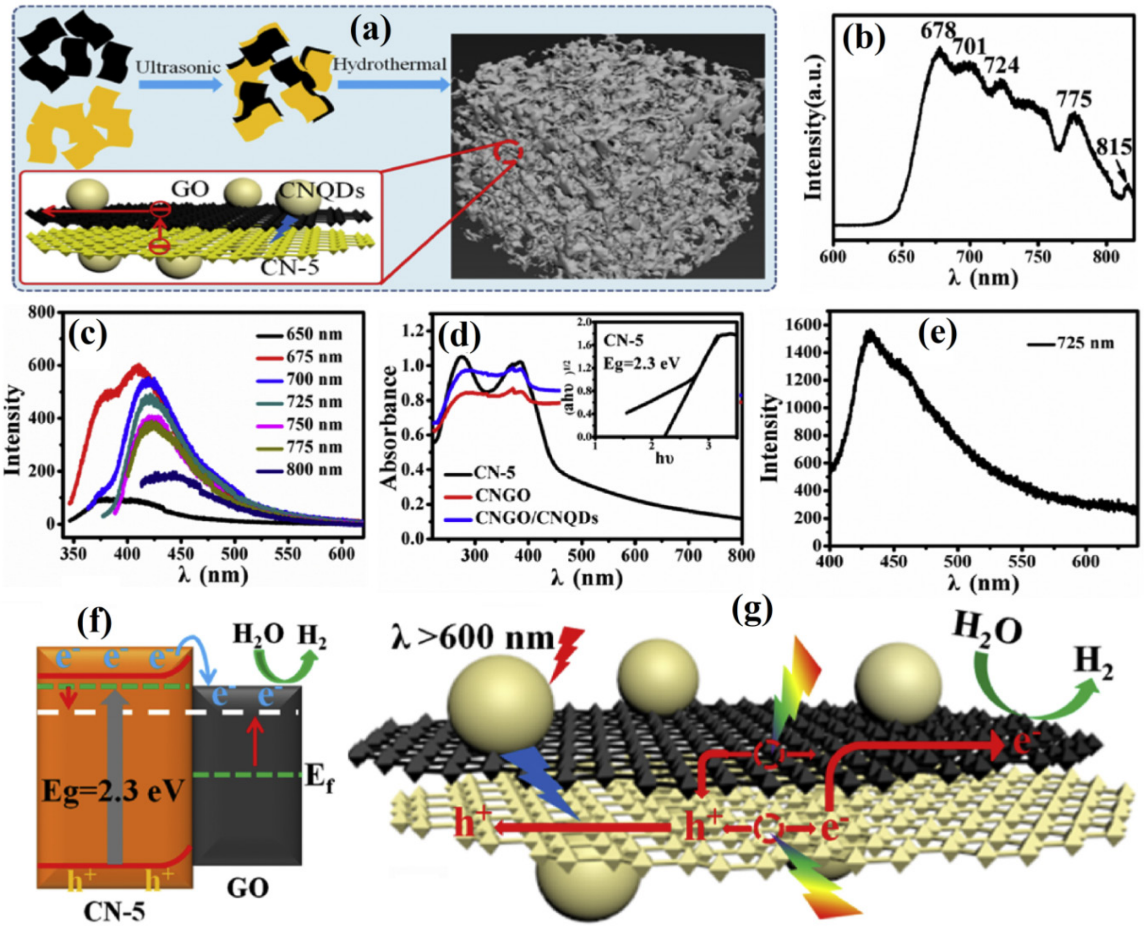

Figure 7. **(a)** Diagrammatic demonstration of the synthetic route of CNGO/CNQDs nanocomposite. **(b)** UC PL excitation spectrum of CNQDs at 417 nm excitation wavelength, **(c)** PL results of CNQDs at diverse excitation wavelengths, **(d)** UV-Vis DRS spectra of photocatalysts with the inset showing band gap energy graph ((ahν)$^{1/2}$ *vs.* photon energy (hν)), **(e)** PL spectra of CNGO/CNQDs nanocomposite at 725 nm excitation wavelength and **(f-g)** Diagram representing photocatalytic H_2 generation and photocarriers departure and transferal in CNGO/CNQDs nanomaterials, Reprinted with permission from Elsevier (License No. 5183171313443) [103].

nanocomposite was 1231 µmol h^{-1} which was 16 folds higher compared to the matrix material. Additionally, the observed AQY of CNGO/CNQDs nanocomposite was 13% and 0.116% at 420 nm and 700 nm wavelengths, respectively. CN-5 and GO both formed heterostructure through weak van der Waals forces. Figure 7e illustrates the photocatalytic mechanism of CNGO/CNQDs heterojunction showing photoinduced charge carriers generation under > 600 nm excitation of light. The photoexcited electrons quickly migrated to the GO surface to enrich reactive sites leading to hydrogen production from the H_2O molecule, while holes migrated to the CN-5 surface. Simultaneously, NIR light (with more than 600 nm) was absorbed by CNQDs, which in reverse emitted light that CN-5CN-5CN-5CN-5 absorbed absorbed absorbed absorbed through the UC process enabling more photocatalytic H_2 production from UV-NIR. Plausible photocatalytic H_2 production mechanism and photocarriers separation and transferal process of CNGO/CNQDs nanocomposite were shown in Figure 7(f-g).

Qin and Zeng also reported the fabrication of Ag/CQDs/g-C_3N_4 nanocomposite by the deposition of plasmonic Ag NPs on CQDs/g-C_3N_4 for full solar spectrum utilized H_2 production [104]. The prepared unique and novel nanocomposite exhibited favorable properties, *i.e.* SPR and

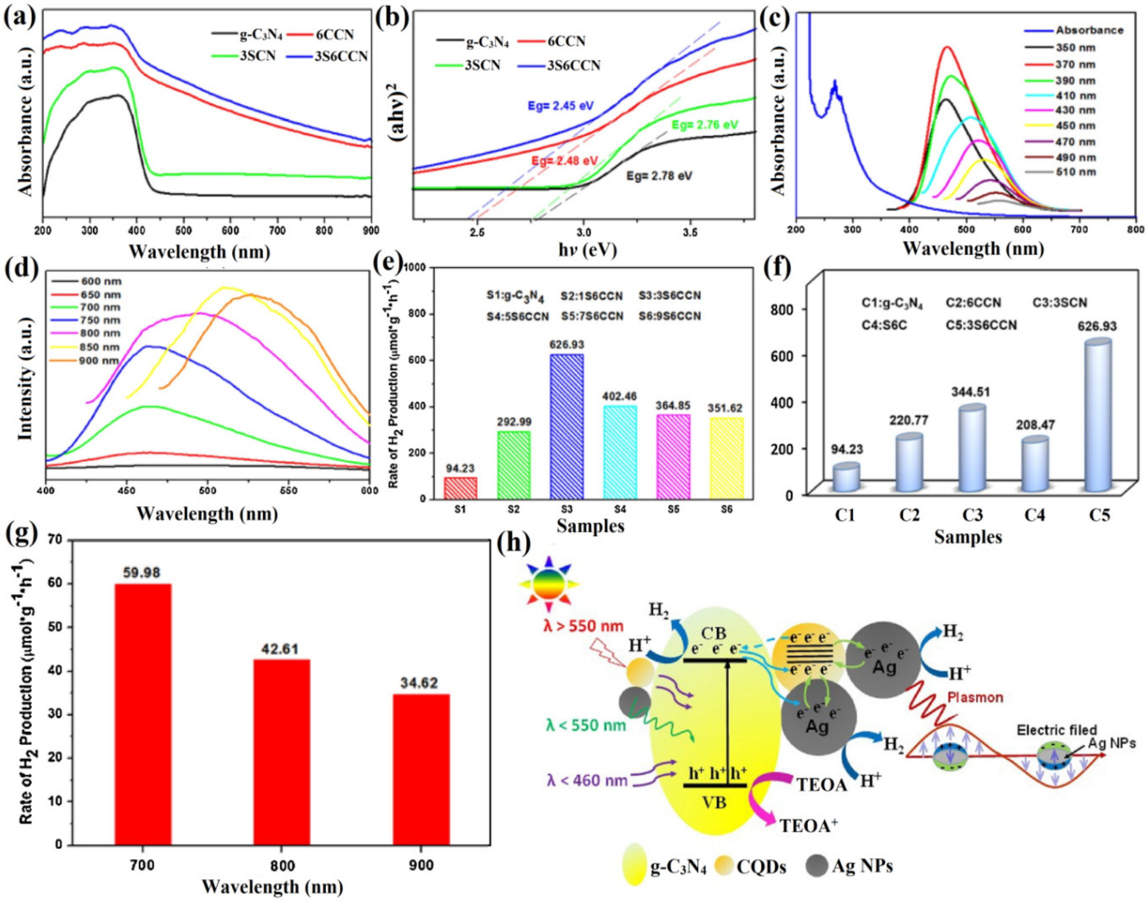

Figure 8. **(a)** UV–vis DRS and **(b)** (ahν) vs. hν curve of g-C_3N_4, CQDs/g-C_3N_4 (6CCN), Ag/g-C_3N_4 (3SCN) and Ag/CQDs/g-C_3N_4 (3S6CCN), **(c)** UV-vis absorption and down-converted PL spectra and **(d)** UC PL spectra synthesized CQDs. Photoactivity of all photocatalysts showing H_2 generation/evolution rates (HER) of **(e)** pure g-C_3N_4 and Ag NPs modified 6CCN (6 mL CQDs/g-C_3N_4) nanocomposites with different amounts and **(f)** optimum samples of unary (g-C_3N_4), binary (CQDs/g-C_3N_4, Ag/g-C_3N_4, Ag/CQDs) and ternary (Ag/CQDs/g-C_3N_4), **(g)** HER of 3S6CCN nanocomposite under 3 h of NIR monochromatic light exposure, *i.e.* 700 nm, 800 nm or 900 nm. **(h)** Proposed mechanistic illustration of photoexcited charge carriers generation and transmission by Ag/CQDs/g-C_3N_4 nanocomposite displaying photocatalytic H_2 production, Reprinted with permission from Elsevier (License No. 5183180007526) [104].

UC PL effect by Ag NPs and CQDs to prolong light harnessing of g-C_3N_4 towards the NIR region. In the interim, Ag NPs and CQDs both served as electron sinks, resulting in enhanced photocarriers departure efficiency and increased quantum proficiency of g-C_3N_4. UV-Vis-NIR DRS spectra of all samples were shown in Figure 8a displaying a red shift in light absorption edge of both 6CCN (6 mL CQDs/g-C_3N_4) and 3S6CCN (3 wt% Ag amended 6 mL CQDs/g-C_3N_4) nanocomposite due to π- π* and n-π* transitions of carbons nanoparticles. The extended light absorption towards the NIR region clarified the successful coupling of CQDs with other g-C_3N_4. With the amendment of CQDs, the band gap (E_g) of 3S6CCN nanocomposites significantly reduced to 2.45 eV from 2.78 eV (Figure b), which was apt for visible and even NIR light absorption to increase H_2 evolution and AQY. For more explanation and to validate the advantage of CQDs, UV-vis absorption and down-converted PL spectra, as well as UC PL belongings of CQDs, were explored at several excitation wavelengths, as can be seen in Figures 8c and d. UC PL spectra of CQDs confirmed light-harvesting in visible (600-700 nm) and NIR (700-900 nm) regions with the emission of shorter wavelength (400–550 nm) visible light owing to a multiphoton active method. Beneath visible light exposure, the photocatalytic H_2 generation rate of 3S6CCN nanocomposite was 626.93 μmol g^{-1} h^{-1} and was approx. 6.7 and 2.8 folds more than bare g-C_3N_4 and CQDs/g-C_3N_4 nanocomposite individually (Figure 8(e-g)). Similarly, under NIR light exposure at 700, 800, or 900 nm wavelength, obtained H_2 production rate by 3S6CCN was 59.98, 42.61, and 34.62 μmol $g^{-1}h^{-1}$, respectively. A proposed photocatalytic process for light-assisted aqueous protons reduction by Ag/CQDs/g-C_3N_4 heterostructure was illustrated in Figure 8h. The combined influence of CQDs and Ag NPs played a significant role in the conversion of longer wavelengths of sunlight to smaller wavelengths *via* the UC process. UC process resulted in the excitation of g-C_3N_4 or Ag/g-C_3N_4 photocatalysts to generate photocarriers and validated the role of CQDs as a photosensitizer. Simultaneously, Ag NPs also exhibited an SPR effect that increased the light harnessing capacity of CQDs towards the NIR region.

3.2. g-C_3N_4 based UC nanomaterials for pollutant degradation

3.2.1. Ln doped UC NPs/g-C_3N_4 nanomaterials

Many researchers have synthesized g-C_3N_4 based UC nanomaterials for the removal of several pollutants present in water. Some of the reports are elucidated in this section, such as Zhang *et al.* reported the fabrication of plasmonic Au NPs and $NaYF_4$:Yb^{3+}, Er^{3+}, Tm^{3+} microsphere (NYF MSs) UC NPs decorated g-C_3N_4 NSs (Au-NYF/g-C_3N_4) *via* the facile one-step in-situ process for methyl orange (MO) degradation [105]. The decorated Au-NYF on g-C_3N_4 NSs surface resulted in higher NYF yield and strong interaction among NYF and g-C_3N_4 in which g-C_3N_4 NSs acted as a support for both NYF MSs and Au NPs shown in HRTEM results (Figure 9a). The prepared Au-NYF/g-C_3N_4 nanomaterials displayed superior stability and extensive light absorption towards extended solar spectrum (UV-visible-NIR) leading to enhanced photodegradation ability than bare g-C_3N_4. Optical possessions of prepared photocatalysts were analyzed by UV-Vis-NIR DRS studies exhibiting extended light-harvesting in the NIR region (900 to 1000 nm) by NYF, NYF/g-C_3N_4, and 1 wt % Au-NYF/g-C_3N_4 as represented in Figure 9b. A distinct absorption band perceived in the NIR range at around 980 nm was due to the ${}^2F_{7/2} \rightarrow {}^2F_{5/2}$ transition of Yb^{3+} ions in $NaYF_{4,}$ and an additional peak at 550 nm was 1 wt % loading of Au NP (SPR excitation). Similarly, UC photoluminescence (PL) spectra of photocatalysts revealed emission peaks of NYF at around green 521 (${}^2H_{11/2} \rightarrow {}^4I_{15/2}$ by Er^{3+} ion), 540 nm (${}^4S_{3/2} \rightarrow {}^4I_{15/2}$ by Er^{3+} ion), 477 (${}^1G_4 \rightarrow {}^3H_6$ by Tm^{3+} ion), 451 nm (${}^1D_2 \rightarrow {}^3F_4$ by Tm^{3+} ion), 361 (${}^1D_2 \rightarrow {}^3H_6$ by Tm^{3+} ion) and 345 nm (${}^1I_6 \rightarrow {}^3F_4$ by Tm^{3+} ion) (Figure 9c). Identical emission peaks were observed for NYF/g-C_3N_4, and 1 wt % Au-NYF/g-C_3N_4 nanocomposites. Additionally, Au NPs and NYF had a negligible effect on MO degradation inferring that both SPR effect (Au NPs) and UC (NYF) were not able to directly activate the photodegradation reaction under solar light exposure (Figure 9d). Hence, a major role of g-C_3N_4 was observed during photocatalytic degradation of MO. The photocatalytic mechanism and energy transfer routes of Au-NYF/g-C_3N_4 NIR-responsive nanocomposite were shown in Figure 9(e, f) under 980 nm light irradiation. Photodegradation results displayed superior photodegradation ability by 1 wt % Au-NYF/g-C_3N_4 *i.e.* 83% against MO under light exposure and the major reactive species were $^{\bullet}O_2^-$ and $^{\bullet}OH$ radicals verified through scavenging experiment. The incremented photoremoval efficacy of Au-NYF/g-C_3N_4 nanocomposite was due to increased charge carriers' departure and migration. Energy transfer routes represented consecutive energy transmission from Yb^{3+} to Er^{3+} and from Yb^{3+} to Tm^{3+}.

Similarly, full-spectrum driven barbituric acid doped g-C_3N_4 coupled with BiF_3:Yb^{3+}, Er^{3+} UC NPs (BFY/$CNB_{0.5}$) were synthesized by Zhang and coworkers for the removal of RhB [106]. The BFY/$CNB_{0.5}$ nanocomposites exhibited superior photocatalytic efficacy than bare g-C_3N_4 which was verified through photodegradation results. The improved photoremoval efficacy was due to harvesting of full solar spectrum energy and enhanced charge carrier separation. The observed removal efficacy by BFY-2/$CNB_{0.5}$ for RhB was 99.4% (within 30 min) and 64.7% (within 80 min) of visible and NIR light irradiation, respectively. Also, RhB removal efficacy under simulated solar light was 98.0% within 15 min by BFY-2/$CNB_{0.5}$. The plausible photocatalytic pathway is illustrated in Figure 10a. UV-vis-NIR DRS and UC PL result explored that BFY UC NPs Yb^{3+} ions absorbed photons beneath NIR light exposure and exhibited ${}^2F_{7/2} \rightarrow {}^2F_{5/2}$ transition

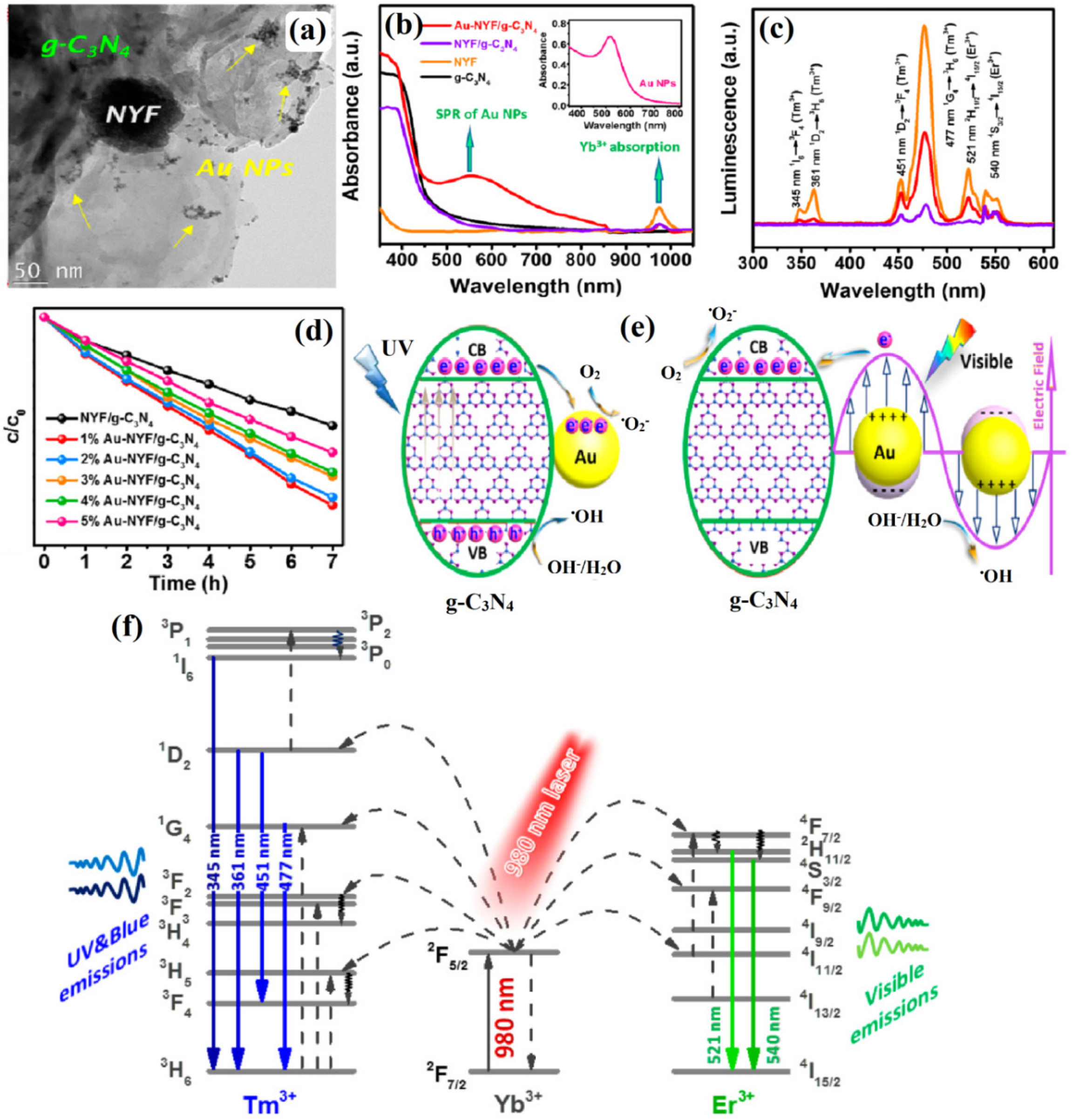

Figure 9. **(a)** TEM picture of 1 wt% Au-NYF/g-C_3N_4 photocatalyst, **(b)** UV-vis-NIR absorption spectra (inset showing absorption spectrum of Au NPs in H_2O), and **(c)** UC PL spectra of synthesized photocatalysts. **(d)** Photodegradation results of MO using synthesized photocatalysts and **(e)** Possible photodegradation mechanism of Au-NYF/g-C_3N_4 nanocomposite beneath UV and visible light ($\lambda > 475$ nm) exposure. **(f)** Energy transfer diagrams showing UC excitation and UV-vis light emissions by NYF under 980 nm laser NIR light exposure, Reprinted with permission from American Chemical Society (Copyright©2017) [105].

afterwards energy was transported to Er^{3+} *via* ET process and $^4I_{11/2} \rightarrow {}^4F_{7/2}$, $^4I_{13/2} \rightarrow {}^4F_{9/2}$, $^4I_{15/2} \rightarrow {}^4I_{11/2}$, $^4S_{3/2} \rightarrow {}^4I_{15/2}$, $^4F_{9/2} \rightarrow {}^4I_{15/2}$, $^2H_{9/2} \rightarrow {}^4I_{15/2}$, $^2H_{11/2} \rightarrow {}^4I_{15/2}$, transitions were formed by Er^{3+} ions. Another report on BiOBr:Yb^{3+},Er^{3+}/g-C_3N_4 (BYE/GCN) p-n heterostructure was published by Liang *et al.* [107]. In this report, doped Yb^{3+}, Er^{3+} ions had efficiently extended absorption of BiOBr towards the NIR region by UC emission from NIR to UV through Er^{3+} (UC transition). Apt band edge positioning of BYE and g-C_3N_4 photocatalysts facilitated photocarriers departure efficacy and boosted RhB degradation rate in visible or NIR light illumination. Optical results

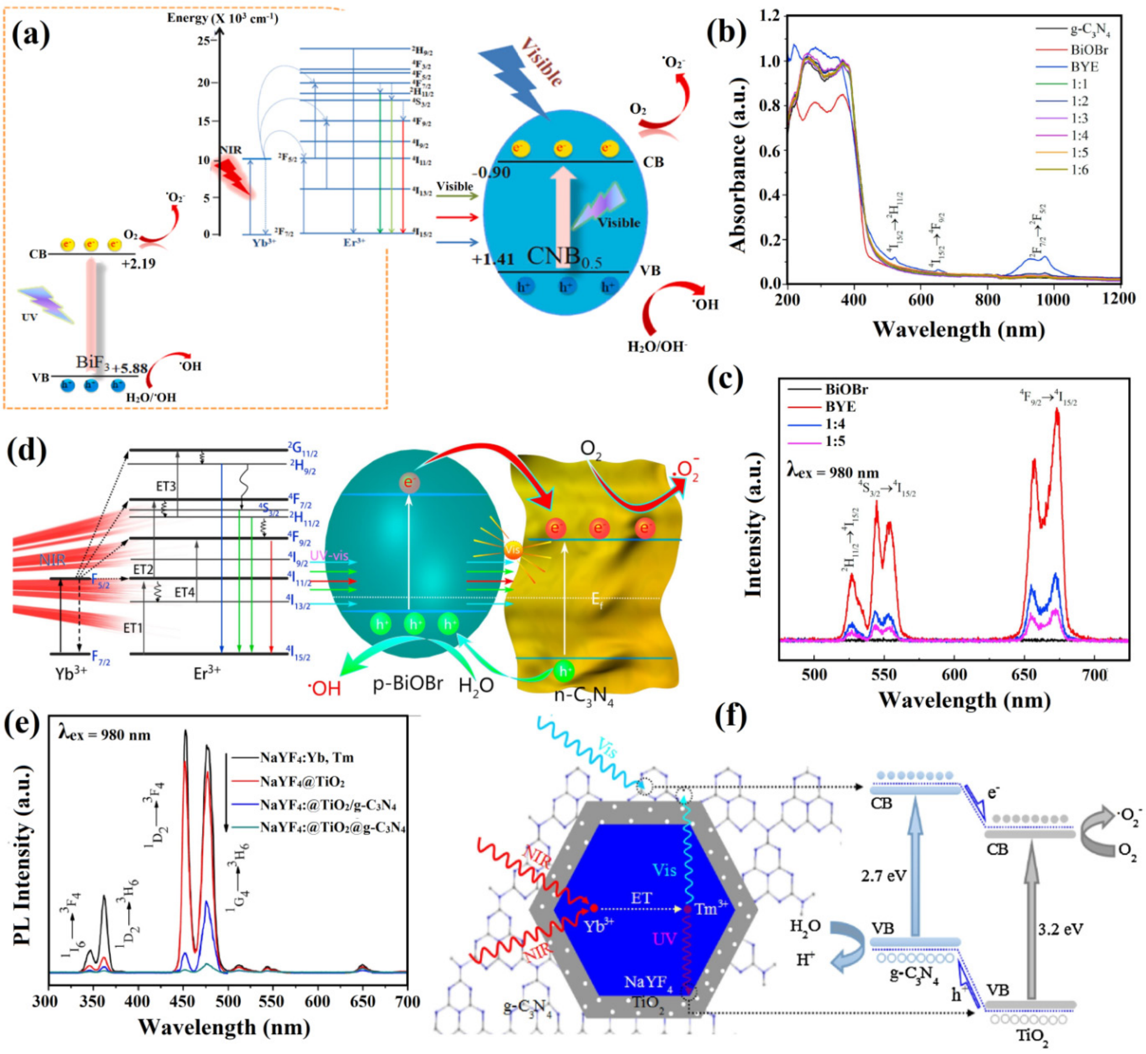

Figure 10. **(a)** Possible photodegradation route of BFY/CNB$_{0.5}$ nanocomposite beneath simulated sunlight exposure [106]. **(b)** UV–Vis-NIR absorption results of different photocatalysts, **(c)** UC emission results of BiOBr, BYE, and BYE/GCN photocatalysts beneath 980 nm laser, and **(d)** Proposed photocatalytic process of BYE/CN p-n junction in the presence of visible and NIR light illumination with energy transfer UC mechanism [107]. **(e)** UC spectra of different fabricated photocatalysts (NaYF$_4$:Yb,Tm, NaYF$_4$@TiO$_2$, NaYF$_4$@TiO$_2$/g-C$_3$N$_4$, and NaYF$_4$@TiO$_2$@g-C$_3$N$_4$) under 980 nm excitation and Probable working photocatalytic process of NaYF$_4$@TiO$_2$@g-C$_3$N$_4$ nanocomposite [108], Reprinted with permission from Elsevier (License No. 5183180560313, 5183180731175 and 5183180916545).

(UV-vis-NIR DRS) of bare BiOBr, BYE, g-C$_3$N$_4$ and BYE/GCN photocatalysts were shown in Figure 10b. Characteristic absorption peaks around 520 and 660 nm were observed in Er/Yb co-doped nanocomposite owed to Er^{3+} excitation causing 4f electronic transition from $^4I_{15/2} \rightarrow {}^2H_{11/2}$ $^4I_{15/2} \rightarrow {}^4F_{9/2}$, individually beneath visible light exposure. Figure 10c indicated typical UC emission spectra (450-750 nm) of all prepared photocatalysts under 980 nm NIR laser. Also, the UC process (by Er^{3+} ion), Yb^{3+} ion instigated dye sensitization effects and transference of energy from Yb^{3+} to Er^{3+} ions. Figure 10c illustrates the RhB degradation mechanism beneath NIR light exposure. Similar transitions were perceived for Er^{3+} as discussed in previous examples. ET mechanism shown in Figure 10d illustrated absorption of ~980 nm NIR light by Er^{3+} and Yb^{3+} ions resulting in UV and visible light emission *via* UC route. The emitted light caused the excitation of p-BiOBr and n-C3N4 photocatalyst to produce photoexcited charge carriers, leading to ROS production. As a result, produced $•O_2^-$, •OH radicals carried out further photocatalytic reactions beneath NIR light exposure. Likewise, Cheng *et al.* prepared g-C3N4/NaYF4:Yb,Tm@TiO2 ternary nanocomposite, exhibiting improved Vis/NIR-driven photodegradation efficiency [108]. The obtained outcomes indicated that UC $NaYF_4$:Yb,Tm NCs were proficient in prolonging the light harnessing ability of g-C_3N_4 towards the NIR range owing to heterojunction formation and UC effect. UC spectra of all-synthesized photocatalysts are shown in Figure 10e. Beneath 980 nm light exposure, peaks observed at 476, 452, 362, and 347nm were attributed to $^1G_4 \rightarrow {}^3H_6$, $^1D_2 \rightarrow {}^3F_4$, $^1D_2 \rightarrow {}^3H_6$, and $^1I_6 \rightarrow {}^3F_4$ transitions of Tm^{3+} ions. Similarly, Yb3+ ions (sensitizer) absorbed NIR photons, and energy was transmitted to Tm^{3+} ions (activator). Due to 3.2 eV and 2.7 eV band gaps of TiO_2 and g-C_3N_4, respectively, UV and visible emissions were absorbed by TiO_2 and g-C_3N_4 to generate photocarriers. The junction amongst TiO_2 and g-C_3N_4 resulted in type II semiconductor heterojunction formation that ultimately produced plenty of ROS ($^•O_2^-$ radicals) to degrade pollutant (Figure 10f).

3.2.2. CQDs UC NPs/g-C_3N_4 nanomaterials

Ultrathin Bi_2WO_6 NSs adorned g-C_3N_4 QDs (CNQDs/BWO), a Z-scheme photocatalyst was fabricated by Zhang and coworkers via hydrothermal route for the exclusion of RhB and TC under full-spectrum light illumination [109]. Optical results of prepared photocatalysts were analyzed through UV-vis DRS analysis as displayed in Figure 11a. Due to absorption edge near 450 nm, BWO photocatalyst exhibited poor visible light absorption, but CNQDs showed extended visible light absorption. The observed absorption curve of CNQDs/BWO nanocomposite displayed a substantial redshift in absorption edge towards the NIR region. The calculated energy gaps of CNQDs and BWO photocatalysts were 2.60 eV and 2.70 eV, respectively, assessed by the Kubelka-Munk equation (Figure 11b). PL emission spectra revealed enhanced transmission and separation of photoinduced charge carriers in 5% CNQDs/BWO nanocomposite owing to low emission peak and red shift (Figure 11c). High intense emission peak referred to the speedy recombination of photocarriers.

Similarly, Figure 11d represented UC spectra of CNQDs at different excitation wavelengths (700, 725, 750, 775, 800, 825, and 850 nm). As the spectra indicated, CNQDs emitted visible light of nearly 430-570 nm under NIR light exposure. The resilient emitted light was obtained at 445 nm upon 750 nm excitation wavelength. The multiphoton active route was the main cause of UC properties in CNQDs due to non-continuous energy among excitation and emission light during the UC process. UC of CNQDs was more advantageous to extending light harnessing capacity and light conversion of the nanocomposite. The degradation results shown in Figure 11e described augmented photodegradation ability of CNQDs/BWO against RhB than bare photocatalysts. The observed TC and RhB removal efficacy by 5% CNQDs/BWO nanocomposite within 60 min of visible light exposure was 87% and 92.51%, respectively. Simultaneously, beneath NIR light illumination, 5% CNQDs/BWO nanocomposite exhibited superior degradation efficacy towards TC, which was 2 folds higher than pure BWO due to UC properties of CNQDs. The proposed visible and NIR-driven photocatalytic mechanism of CNQDs/BWO nanocomposite against TC and RhB degradation was explained in Figure 11f. The mechanism illustrated a Z-scheme pathway under full solar light irradiation.

Also, Feng *et al.* used a simple calcination process to prepare visible-NIR responsive Z-scheme CdS/CQDs/g-C_3N_4 nanocomposites for RhB, MB, and phenol removal by photocatalysis [110]. The fabricated CdS/CQDs/g-C_3N_4 nanoheterostructure displayed extended light-harvesting towards the NIR region, which was proved through UV-vis DRS results (Figure 12a). The observed absorption edges of bare g-C_3N_4 and CdS were around 471 and 590 nm due to the inherent E_g of g-C_3N_4 and CdS, respectively, while the observed direct E_g values for 2S5CCN, CdS, and g-C_3N_4 photocatalysts were 2.68 eV, 2.24, and 2.79 correspondingly (Figure 12b). The 2SCN, 5CCN, and 2S5CCN nanocomposite presented a strong red shift in absorption edges and wide light absorption at 482, 491, and 503 nm towards the NIR region formation of Z-scheme CdS/CQDs/g-C_3N_4 heterostructure. Similarly, the UC PL property (Figure 12c) revealed excitation wavelength-dependent fluorescence capability of CQDs, showing absorption towards longer wavelengths in the

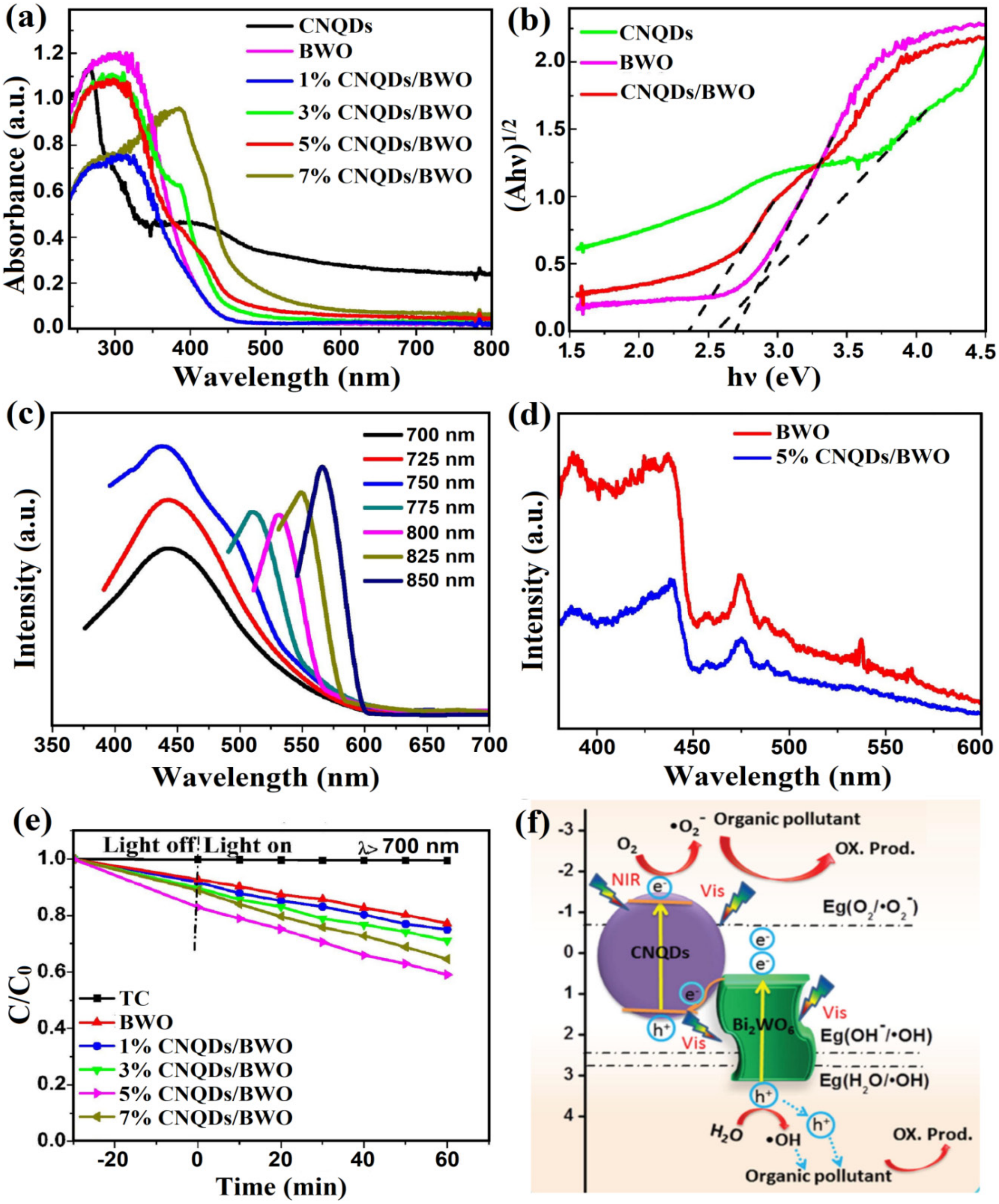

Figure 11. **(a)** UV-vis DRS spectra, **(b)** band gap analysis of synthesized photocatalysts, **(c)** PL spectra, and **(d)** UC PL spectra of CNQDs under 700 to 850 nm excitation wavelengths. **(e)** Photodegradation results of prepared photocatalysts towards TC removal under NIR light illumination and **(f)** Graphic representation of plausible Z-scheme mechanism of CNQDs/BWO nanocomposite under full solar light radiation, Reprinted with permission from Elsevier (License No. 5183181091964) [109].

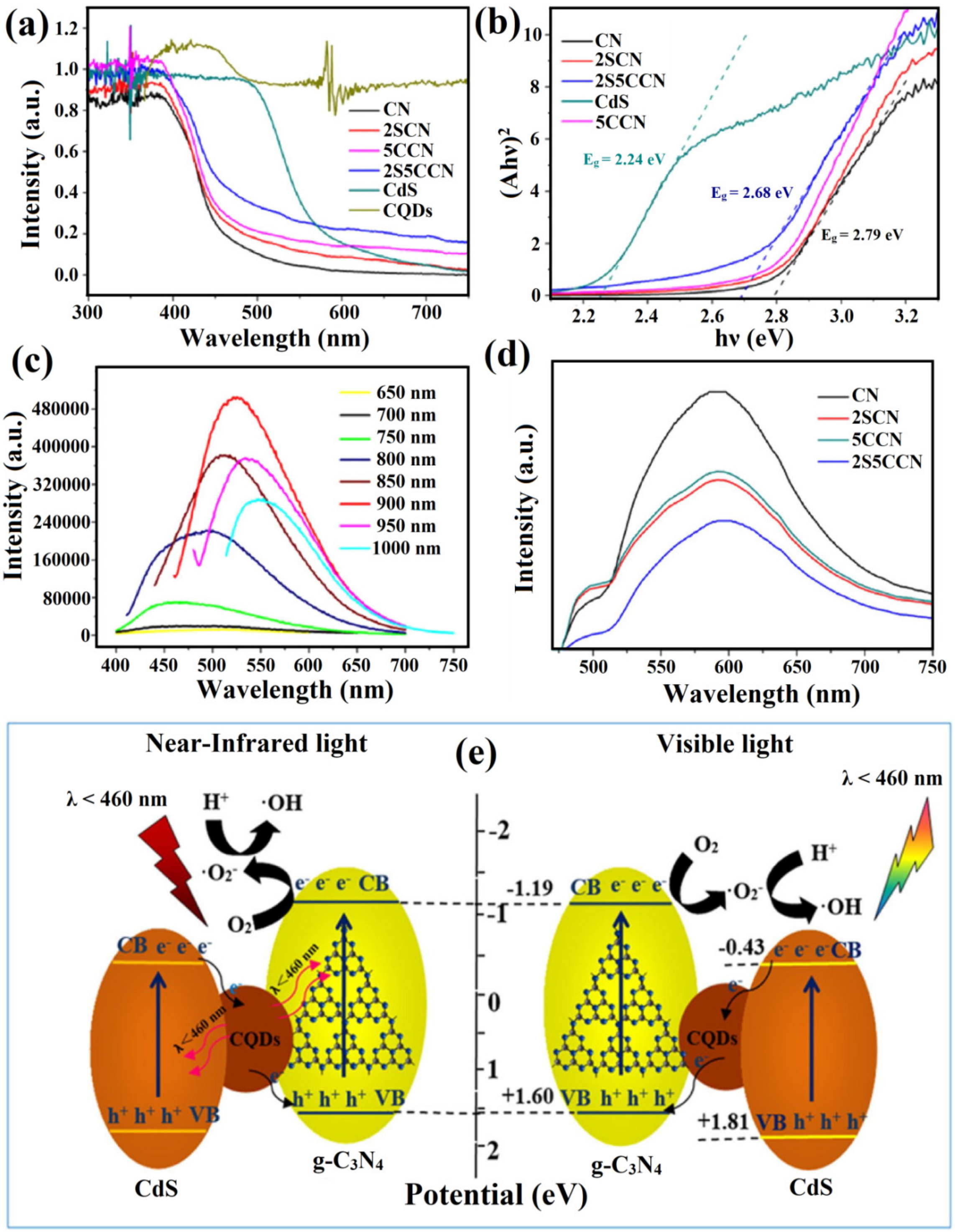

Figure 12. **(a)** UV–vis DRS results and **(b)** $(ah\nu)^2$ vs. hν curve of synthesized photocatalysts (g-C_3N_4(CN), bare CdS, CdS(0.25%)/g-C_3N_4 (2SCN), CQDs(0.5%)/g-C_3N_4 (5CCN) and CdS(0.25%)/CQDs(0.5%)/g-C_3N_4(2S5CCN)), **(c)** UC PL results of fabricated CQDs at diverse wavelength, **(d)** PL spectra of CN, 2SCN, 5CCN photocatalysts and (e) Z-scheme pathway mechanism showing energy band diagram and charge transferal in CdS/CQDs/g-C_3N_4 nanocomposite, Reprinted with permission from Elsevier (License No. 5183181280297) [110].

range 650–750 nm (visible) and 800–1000 nm regions with the emission of lower wavelength light from 400–600 nm. As previously discussed, the reason for the UC PL property of CQDs were multiphoton active course and their efficient connection with one another. CQDs also acted as photosensitizers in CdS/CQDs/g-C_3N_4 nanocomposite to efficiently absorb the full solar spectrum and enhance photodegradation ability. The Z-scheme charge transmission was also confirmed through PL emission analysis (Figure 12d), as all the synthesized samples had identical emission bands at 550-650 nm with 467 nm excitation wavelength. Lower PL peak intensity of 2SCN nanocomposites also verified a decrease in photocarriers recombination rate compared to pristine g-C_3N_4 after the incorporation of CdS NPs. Likewise, the lowest peak intensity of 2S5CCN nanocomposite than all photocatalysts confirmed high charge carriers separation and transmission due to CQDs. The synthesized nanocomposite has apt energy band gap alignment among photocatalysts resulting in the formation of a Z-scheme nanocomposite in which CdS was joined with g-C_3N_4 via an electron intermediary CQDs. The CQDs as an electron moderator assisted and enhanced transportation and separation of charge carriers with high redox ability (oxidize ability) in Photodegradation results verified increased photoactivity and photostability of CdS/CQDs/g-C_3N_4 nanocomposite under NIR light irradiation compared to bare and binary photocatalysts. The superior photodegradation ability of 2S5CCN nanocomposite was observed against RhB, Mb, and phenol pollutants which were 100% (within 20 min), 98% (within 120 min), and 58% (within 120 min) under visible light exposure. Correspondingly, beneath NIR light (k > 820 nm) exposure, 38% and 62% RhB removal efficacy were observed by 5CCN and 2S5CCN nanocomposite, respectively. The possible RhB, MB, and phenol photodegradation mechanisms presenting the Z-scheme charge transferal pathway under NIR and visible light illumination are shown in Figure 12e. Mechanism explored adequate prolonged solar light (NIR light) absorption by nanocomposite due to CQDs exhibiting UC fluorescence properties. The major reactive species contributing to the photochemical reaction were $^{\bullet}O_2^-$ and $^{\bullet}OH$ radicals, also verified through scavenging experiments.

4. Conclusion

In summary, we can conclude that the high demand for photocatalytic wastewater treatment and energy production has gathered the interest of researchers worldwide. Therefore, different UV and visible light-responsive photocatalysts have been explored for pollutant degradation and energy production. But incomplete solar spectrum utilisation has restricted the applicability of wide band gap and visible light active photocatalysts in photocatalytic fields. Recently, NIR-driven semiconductors have gained much consideration in pollutant degradation and hydrogen production. The solar spectrum has a maximum portion of NIR light, i.e. ~52%, compared to UV (~5%) and visible light (~ ~ ~43%). Henceforth, many strategies have been employed for complete solar spectrum utilization and to make photocatalyst as NIR active photocatalyst, such as UC, band gap engineering, surface plasmon resonance, photosensitization, and heterostructure formation with narrow band gap photocatalysts. In this review, we have highlighted the UC strategy by incorporating lanthanides (Ln^{3+}) as dopants and coupling with CQDs as the primary strategy to fabricate NIR-driven photocatalysts. The Ln^{3+} compounds and CDQs exhibit UC possessions and provide excellent responses to semiconducting materials to extend visible and NIR light absorption. UC process possesses enhanced and efficient photo-redox processes for various upconverted photocatalysts. UC NPs doped with Ln^{3+} ions and CQDs produce UV and visible light emissions under NIR light excitation. Ln^{3+} ions are the main UC nanomaterials to attain spectral conversion because of rare-earth elements' distinctive 4f electronic configuration. Under NIR light illumination, GS photons of sensitizer excited to ES of activator/annihilators ions which caused non-radiative or radiative relaxation of the population to activator ions of GS to succeed UC emission. CQDs show up-and down-converted PL properties and excellent photo-excited electron migration ability, which contribute to strong NIR harnessing.

Other than Ln^{3+} and CQDs-based UC materials, we have a brief discussion on TTA based UC mechanism. As a photocatalyst, in this review, we have selected a metal-free and visible-light-driven g-C_3N_4 photocatalyst for literature discussion due to many unique properties such as apt bandgap, high thermochemical stability, low cost and ecofriendly which are beneficial for various photocatalytic applications. But, low visible light absorption (460 nm) of g-C_3N_4 due to the 2.7 eV energy gap restricts full solar light harvesting property. So, we have discussed UC as an effective NIR strategy to boost the light-harvesting capacity of g-C_3N_4 via incorporating Ln^{3+} dopants and CQDs nanomaterials. Previously, the UC strategy has been engaged by researchers to modify and extend the light absorption ability of g-C_3N_4 in the NIR region. The summarized data on the photocatalytic application of g-C_3N_4 based NIR driven UC nanomaterials for H_2 production and pollutant degradation is shown in Table 1. The review also précised the latest development of NIR-responsive g-C_3N_4 based UC photocatalysts with their upconverted photocatalytic mechanism.

4.1. Future challenges and perspectives

Despite UC nanomaterials' advantage in extending the light absorption ability of photocatalysts towards the NIR region (UV-visible to NIR), many challenges should be considered as their use in the photocatalysis field is just in progress. The UC based NIR photocatalysis is a developing technique with new electrifying opportunities. Though UC nanomaterials are of great potential still, UC NPs have many limitations in their practical applications, which have been discussed below:

- Ln^{3+} doped UC nanomaterials have low absorption ability. For example, Yb^{3+} ions are mostly used UC nanomaterial, which acts as a sensitizer and exhibits only a narrow band positioned at 980 nm. In recent times, some the sensitizers like Nd^{3+} ions have been discovered and have gained a lot of interest due to their strong absorption at around 808 nm. It has shown low absorption by water at 808 nm with high absorption cross-sections.
- In photocatalytic wastewater treatment, there is the requirement for more UC NPs, which can be sensitized by various kinds of dopants. Similarly, a combination of UC nanomaterials with diverse sensitizer dopants also needs more exploration for efficient and prolonged light absorption. Other than this, the incorporation of specific nanomaterials such as synthetic dyes, transition metals, and QDs with high absorption cross-sections is a more effective way that can be employed to prolong light absorption capacity *via* wide-ranging light excitation.
- In addition, the effectual contact of UC NPs with natural solar light is still a big challenge/problem. Therefore, for the NIR active photocatalytic process, lasers with limited light ranges or focused solar light are highly needed to act as an effective light illumination source.
- Another challenge in UC nanomaterials-based nanocomposite is its charge/energy transfer (ET) mechanism inside UC NPs, among UC NPs and sensitizers, and amid UC NPs which is a very sophisticated and inexplicable and need more investigation. To better recognise difficult ET routes, the path and time measurement of energy flow must be known.
- Low quantum yields (QY) of the UC NPs are another task that UC communal is facing. Henceforth, Tm^{3+}, $Er^{3+,}$ and Tm^{3+}/Er^{3+} ions are the most used activators for effective UC process due to utmost internal QY. For example, 7.6% QY was observed for $LiLuF_4$:Yb/Tm@$LiLuF_4$ NPs under light irradiation of 127 Wcm^2. Low energy transfer efficacy from sensitizer to the activator, quenching of UC PL through cross-relaxation, and energy losses owing to surface defects are the main reasons behind low UC QY.
- To understand the whole UC process (charge or energy transfer mechanism), the development of some advanced ultrafast characterization methods, organized/modified synthetic strategies, and theoretical studies are highly required. Density functional theory (DFT) studies (computational quantum mechanical modeling method) should be performed to better understand the electronic structure (mainly the ground state), particularly in atoms, molecules, and condensed phases.
- Various UC NPs have been fabricated and employed in different fields. In photocatalysis, most of the reports on UC NPs were either for pollutant degradation or for H_2 production *via* water splitting, and few were on artificial photosynthesis. Nowadays, global warming and energy crisis are the major issues. Therefore, research on photocatalytic H_2O splitting, O_2 evolution, and CO_2 reduction using UC photocatalysts is urgently required. Besides this, research on Cr(IV) reduction

S.No.	Photocatalysts	UC NPs as NIR light harvester	Synthesis method	NIR light sources	Enhanced wavelength	Hydrogen production rate and Photodegradation efficiency (%)	Ref.
Hydrogen Production							
1.	**15 wt% NYFG/C$_3$N$_4$ NT**	**NaYF$_4$:Yb,Tm,Gd (NYFG)**	Facile chemical technique	980 nm laser irradiation	300-1100 nm	311.6 μmol g^{-1}	[58]
2.	Au-PtDPA@ SiO$_2$@0.5NC2	**Au-PtDPA@SiO$_2$**	Hydrothermal method	a xenon lamp (300 W) and UV-cut-off filter (780 nm > λ > 420 nm)/green light	300-700 nm	16.88 μmol g^{-1}	[81]
3.	UCN/CQDs-0.2%	**CQDs**	Hydrothermal method	A 300 W Xe-lamp with a 420 nm cutoff filter	300-800 nm	88.1 μmol h^{-1}	[97]
4.	UCNPs@SiO$_2$@ Ag/g-C$_3$N$_4$	**NaLuF$_4$:Gd,Yb,Tm@ NaLuF$_4$:-Gd,Yb (UCNPs)**	Sonication	A 300 W Xe lamp	300-800 nm	873 μmol h^{-1}g^{-1} and 100% Rhodamine B removal within 90 min	[100]
5.	NaYF$_4$:Yb/Tm@ Ag$_3$PO$_4$/Ag@g-C$_3$N$_4$	**NaYF$_4$:Yb/Tm**	A facile ultrasonication	A 300 W Xe lamp	300-1100 nm	23.56 μmol g^{-1}h^{-1}	[101]
6.	CNQD-g-C$_3$N$_4$	**CNQD**	A thermal-chemical etching process	A 600 nm cut-off filter	200-800 nm	109.96 μmol g^{-1}h^{-1}	[102]
7.	CNGO/CNQDs	**CNQDs**	Hydrothermal and vacuum injection method	A 300 W xenon lamp	200-800 nm	1231 μmol h^{-1}	[103]
8.	Ag/CQDs/g-C$_3$N$_4$	**CQDs**	Chemical reduction method	A 300 W Xe lamp	200-900 nm	626.93 μmol g^{-1}h^{-1}	[104]
Pollutant degradation							
9.	**β-NaYF$_4$:Yb^{3+}, Tm^{3+}/g-C$_3$N$_4$**	β-NaYF$_4$:**Yb^{3+}, Tm^{3+}**	Stepwise method	980 nm laser irradiation	200-1200 nm	83% removal of Methylene Blue within 6h	[60]
10.	Er^{3+} doped g-C$_3$N$_4$	**Er^{3+} ions**	In situ synthesis approach	A white LED (λ > 420 nm) and A red laser (640−660 nm)	200-900 nm	100% removal of Rhodamine B within 40 min	[75]
11.	NaYF$_4$: Yb, Er/ g-C$_3$N$_4$	**NaYF$_4$: Yb, Er**	A facile two-step route	980 nm laser irradiation	200-900 nm	-	[76]
12.	40% CeF$_3$/g-C$_3$N$_4$	**CeF$_3$**	Microwave hydrothermal method	LED lamp (770 nm < λ < 860 nm) irradiation	250-700 nm	84.2% removal of Dibenzothiophene within 3 h	[77]
13.	Ag$_2$CrO$_4$/N-GQDs@g-C$_3$N$_4$	**N-GQDs**	Freeze-drying and reflux method	A 300W Xe lamp with 420 nm and 760 nm cutoff filters	200-800 nm	39.9% removal of Doxycycline within 120 min	[98]

14.	3%NGQDs-60%C_3N_4/ Bi_2WO_6	**NGQDs**	Facile hydrothermal method	250 W xenon lamp with a 420 nm cutoff filter and 150 W infrared lamp	200-700 nm	29.8% removal of Tetracycline after 180 min	[99]
15.	Au-NYF/g-C_3N_4	**$NaYF_4$;Yb^{3+}, Er^{3+}, Tm^{3+} (NYF)**	A single step via in situ synthesis	A 980 nm diode laser	3200-1000 nm	83% removal of Methyl orange within 7h	[105]
16.	BFY-2/$CNB_{0.5}$	**BiF_3;Yb^{3+}, Er^{3+} (BFY)**	In-situ synthesis	A 300W Xe lamp	300-1200 nm	98.0% removal of Rhodamine B within 15 min	[106]
17.	BiOBr: Yb^{+3}, Er^{+3}/g-C_3N_4 (BYE/CN)	**Yb^{+3}, Er^{+3}**	Stepwise method	A 300W Xenon lamp	200-1200 nm	29% removal of Rhodamine B after 12 h	[107]
18.	$NaYF_4$:Yb,Tm@ TiO_2/g-C_3N_4	**$NaYF_4$;Yb,Tm**	One-pot hydrothermal method	980 nm NIR laser	400-1200 nm	Rhodamine B	[108]
19.	CNQDs/BWO	**CNQDs**	Hydrothermal reaction	A 300W Xe lamp	200-800 nm	87% and 92.51% TC and RhB removal within 60 min	[109]
20.	CdS/CQDs/g-C_3N_4 (2S5CCN)	**CQDs**	Simple calcination process	A 300W Xe lamp	300-700 nm	98 % and 58% removal of Methylene Blue and Phenol within 120 min	[110]

Table 1. Photocatalytic applications of NIR activated g-C_3N_4 based upconversion nanomaterials in H_2 production and pollutant degradation.

and other hazardous pollutants (pesticides, antibiotics, etc.) removal from wastewater using UC nanomaterials is also needed.

- The UC properties of Ln materials and CDQs also require modifications because they lack the direct photo-conversion efficacy of pristine semiconductors under UV-visible light irradiation. The excited energy liberated via UC PL or through direct transportation of the excited electron from CQDs LUMO level to CB of other semiconductors needs more exploration. The ET process from CQDs to other semiconductors using characterization also requires attention as it is still unclear.

Furthermore, the light absorption ability of NIR active photocatalysts can be enhanced by incorporating plasmonic material as they generate SPR effect, which can concentrate the excitation light source. UC NPs mainly generate UV-visible emissions, which can be utilized for SPR excitation in UV-visible active photocatalysts, ultimately boostingUV-visible emissions production. Thus, the addition of plasmonic materials can extend the NIR photocatalysis process by making the use of UC NPs more effective. In concluding the g-C_3N_4/ UC nanomaterials based NIR photocatalysis, much recent development can be performed in the fabrication of high-quality UC NPs and rational designing of nanocomposite material. UV-active photocatalysts in nanocomposite can also be done since UV photons exhibit much higher energy than visible-NIR photons, which are more advantageous for photocatalysis. Also, the ET process from UC NPs to UV-responsive materials is more efficient than visible-responsive materials. Thus, implementingimplementing the abovementioned viewpoints can enhance the applicability of NIR-based photocatalysts in pollutant degradation and energy conversion processes.

References

[1] Al-Enizi, A.M., Ahmed, J., Ubaidullah, M., Shaikh, S.F., Ahamad, T., Naushad, M., Zheng, G., Utilization of waste polyethylene terephthalate bottles to develop metal-organic frameworks for energy applications: A clean and feasible approach. J. Clean. Prod. 248 (2020) 119251.

[2] Kumar, R., Raizada, P., Khan, A.A.P., Nguyen, V.-H., Van Le, Q., Ghotekar, S., Selvasembian, R., Gandhi, V., Singh, A., Singh, P., Recent progress in emerging $BiPO_4$-based photocatalysts: synthesis, properties, modification strategies, and photocatalytic applications, J. Mater. Sci. Technol. 108 (2022) 208-225.

[3] Ahamad, T., Naushad, M., Ubaidullah, M., Alshehri, S., Fabrication of highly porous polymeric nanocomposite for the removal of radioactive U (VI) and Eu (III) ions from aqueous solution. Polymers, 12(12) (2020) 2940.

[4] Naushad, M., Ahamad, T., Sharma, G., Ala'a, H., Albadarin, A.B., Alam, M.M., ALOthman, Z.A., Alshehri, S.M., and Ghfar, A.A., Synthesis and characterization of a new starch/SnO_2 nanocomposite for efficient adsorption of toxic Hg^{2+} metal ion. Chem. Eng. J. 300 (2016) 306-316.

[5] Lau, V.W., Moudrakovski, I., Botari, T., Weinberger, S., Mesch, M.B., Duppel, V., Senker, J., Blum, V., Lotsch, B.V., Rational design of carbon nitride photocatalysts by identification of cyanamide defects as catalytically relevant sites, Nat. Commun. 7 (2016) 1-10.

[6] Jawed, A., Kar, P., Verma, R., Shukla, K., Hemanth, P., Thakur, V.K., Pandey, L.M., Gupta, R.K., Integration of biological control with engineered heterojunction nano-photocatalysts for sustainable and effective management of water hyacinth weed, J. Environ. Chem. Eng. 10(1) (2022) 106976.

[7] Misra, M., Singh, N., Gupta, R.K., Enhanced visible-light-driven photocatalytic activity of Au@Ag core-shell bimetallic nanoparticles immobilized on electrospun TiO_2 nanofibers for degradation of organic compounds, Catal. Sci. Technol. 7 (2017) 570-580.

[8] Sharma, B., Thakur, S., Mamba, G., Gupta, R.K., Gupta, V.K., Thakur, V.K., Titania modified gum tragacanth based hydrogel nanocomposite for water remediation. J. Environ. Chem. Eng. 9(1)(2021) 104608.

[9] Kumar, R., Sudhaik, A., Khan, A.A.P., Raizada, P., Asiri, A.M., Mohapatra, S., Thakur, S., Thakur, V.K., Singh, P., Current status on designing of dual Z-scheme photocatalysts for energy and environmental applications, J. Ind. Eng. Chem. 106 (2022) 340-355.

[10] Pirhashemi, M., Habibi-Yangjeh, A., Pouran, S.R., Review on the criteria anticipated for the fabrication of highly efficient ZnO-based visible-light-driven photocatalysts, J.Ind.Eng. Chem. 62 (2018) 1-25.

[11] Hasija, V., Kumar, A., Sudhaik, A., Raizada, P., Singh, P., Van Le, Q., Le, T.T., Nguyen, V.-H., Step-scheme heterojunction photocatalysts for solar energy, water splitting, CO_2 conversion, and bacterial inactivation: a review. Environ. Chem. Lett. 19(4) (2021) 2941-2966.

[12] Asadzadeh-Khaneghah, S. and Habibi-Yangjeh, A., g-C_3N_4/carbon dot-based nanocomposites serve as efficacious photocatalysts for environmental purification and energy generation: a review. J. Clean. Prod.276 (2020) 124319.

[13] Sabri, M., Habibi-Yangjeh, A., Rahim Pouran, S., Wang, C., Titania-activated persulfate for environmental remediation: the-state-of-the-art. Catal. Rev. 19 (2021) 1-56.

[14] Fujishima, A., Honda, K.J., Electrochemical photolysis of water at a semiconductor electrode, Nature, 238 (1972) 37-38.

[15] Kar, P., Shukla, K., Jain, P., Sathiyan, G., Gupta, R.K., Semiconductor based photocatalysts for detoxification of emerging pharmaceutical pollutants from aquatic systems: A critical review, Nano Mater. Sci. 3 (2021) 25-46.

[16] Singh, N., Prakash, J., Misra, M., Sharma, A., Gupta, R.K., Dual functional Ta-doped electrospun TiO_2 nanofibers with enhanced photocatalysis and SERS detection for organic compounds, ACS Appl. Mater. Interfaces, 9 (2017) 28495-28507.

[17] Jain, P., Kumar, A., Verma, N., R.K. Gupta, In-situ synthesis of TiO_2 nanoparticles in ACF: Photocatalytic degradation under continuous flow, Sol. Energy, 189 (2019) 35-44.

[18] Kar, P., Shukla, K., Jain,P., Gupta, R.K., Engineering, An activated carbon fiber supported Fe_2O_3@bismuth carbonate heterojunction for enhanced visible light degradation of emerging pharmaceutical pollutants, React. Chem. Eng. 6 (2021) 2029-2041.

[19] Soni, V., Raizada, P., Kumar, A., Hasija, V., Singal, S., Singh, P., Hosseini-Bandegharaei, A., Thakur, V.K., Nguyen, V.-H., Indium sulfide-based photocatalysts for hydrogen production and water cleaning: a review. Environ. Chem. Lett.19(2) (2021) 1065-1095.

[20] Singh, N., Prakash, J., Gupta, R.K., Engineering, Design and engineering of high-performance photocatalytic systems based on metal oxide-graphene-noble metal nanocomposites, Mol. Syst. Des. Eng. 2 (2017) 422-439.

[21] Sharma, S., Dutta, V., Raizada, P., Hosseini-Bandegharaei, A., Singh, P., Nguyen, V.-H., Tailoring cadmium sulfide-based photocatalytic nanomaterials for water decontamination: a review. Environ. Chem. Lett.19(1) (2021) 271-306.

[22] Dutta, V., Sharma, S., Raizada, P., Thakur, V.K., Khan, A.A.P., Saini, V., Asiri, A.M., Singh, P., An overview on WO_3 based photocatalyst for environmental remediation. J. Environ. Chem. Eng. 9(1) (2021) 105018.

[23] Ohko, Y., Ando, I., Niwa, C., Tatsuma, T., Yamamura, T., Nakashima, T., Kubota, Y., Fujishima, A., Degradation of bisphenol A in water by TiO_2 photocatalyst, Environ. Sci. Technol. 35 (2001) 2365-2368.

[24] Zinatloo-Ajabshir, S., Salavati-Niasari, M., Facile route to synthesize zirconium dioxide (ZrO_2) nanostructures: structural, optical and photocatalytic studies, J. Mol. Liq. 216 (2016) 545-551.

[25] Nasseh, N., Taghavi, L., Barikbin, B., Nasseri, M.A., Synthesis and characterizations of a novel $FeNi_3$/SiO_2/CuS magnetic nanocomposite for photocatalytic degradation of tetracycline in simulated wastewater, J. Clean. Prod. 179 (2018) 42-54.

[26] Hasija, V., Raizada, P., Sudhaik, A., Singh, P., Thakur, V.K., Khan, A.A.P., Fabrication of Ag/AgI/WO_3 heterojunction anchored P and S co-doped graphitic carbon nitride as a dual Z scheme photocatalyst for efficient dye degradation. Solid State Sci. 100 (2020) 106095.

[27] Khan, A.A.P., Singh, P., Raizada, P., Asiri, A.M., Converting Ag_3PO_4/CdS/Fe doped C_3N_4 based dual Z-scheme photocatalyst into photo-Fenton system for efficient photocatalytic phenol removal. J. Ind. Eng. Chem. 98 (2021) 148-160.

[28] Jiang, L., Yang, J., Zhou, S., Yu, H., Liang, J., Chu, W., Li, H., Wang, H., Wu, Z., Yuan, X., Strategies to extend near-infrared light harvest of polymer carbon nitride photocatalysts, Coord. Chem. Rev. 439 (2021) 213947.

[29] Yang, M.Q., Gao, M., Hong, M.G., Ho, W., Visible-to-NIR photon harvesting: progressive engineering of catalysts for solar-powered environmental purification and fuel production, Adv. Mater. 30 (2018) 1802894.

[30] Tian, Q. Yao, W., Wu, W., Jiang, C., NIR light-activated upconversion semiconductor photocatalysts, Nanoscale Horiz. 4 (2019) 10-25.

[31] Linsebigler, A.L., Lu, G., Yates Jr J.T., Photocatalysis on TiO_2 surfaces: principles, mechanisms, and selected results, Chem. Rev. 95 (1995) 735-758.

[32] Zhang, Q., Yang, F., Xu, Z., Chaker, M., Ma, D., Are lanthanide-doped upconversion materials good candidates for photocatalysis?, Nanoscale Horiz. 4 (2019) 579-591.

[33] Fan, W., Bai, H., Shi, W., Semiconductors with NIR driven upconversion performance for photocatalysis and photoelectrochemical water splitting, CrystEngComm. 16 (2014) 3059-3067.

[34] Wang, L., Xu, X., Cheng, Q., Dou, S.X., Du, Y., Near-Infrared-Driven Photocatalysts: Design, Construction, and Applications, Small, 17 (2021) 1904107.

[35] Liu, T., Liu, B., Yang, L., Ma, X., Li, H., Yin, S., Sato, T., Sekino, T., Wang, Y., RGO/Ag_2S/TiO_2 ternary heterojunctions with highly enhanced UV-NIR photocatalytic activity and stability. Appl. Catal. B: Environ. 204 (2017) 593-601.

[36] Nakata, K. and Fujishima, A., TiO_2 photocatalysis: Design and applications. J. Photochem.Photobiol. C: Photochem. Rev. 13(3) (2012) 169-189.

[37] Zhu, L., Li, H., Liu, Z., Xia, P., Xie, Y., Xiong, D., Synthesis of the 0D/3D CuO/ZnO heterojunction with enhanced photocatalytic activity. J. Phys. Chem. C, 122(17) (2018) 9531-9539.

[38] Wen, J., Xie, J., Chen, X., Li, X., A review on g-C_3N_4-based photocatalysts. Appl. Surf. Sci. 391 (2017) 72-123.

[39] Sudhaik, A., Raizada, P., Singh, P., Hosseini-Bandegharaei, A., Thakur, V.K., Nguyen, V.-H., Highly effective degradation of imidacloprid by H_2O_2/ fullerene decorated P-doped g-C_3N_4 photocatalyst, J. Environ. Chem. Eng. 8(6) (2020) 104483.

[40] Sudhaik, A., Raizada, P., Thakur, S., Saini, R.V., Saini, A.K., Singh, P., Thakur, V.K., Nguyen, V.-H., Khan, A.A.P., Asiri, A.M., Synergistic photocatalytic mitigation of imidacloprid pesticide and antibacterial activity using carbon nanotube decorated phosphorus doped graphitic carbon nitride photocatalyst. J. Taiwan Inst. Chem. Eng. 113 (2020) 142-154.

[41] Zhao, Z., Sun, Y., Dong, F., Graphitic carbon nitride based nanocomposites: a review, Nanoscale, 7 (2015) 15-37.

[42] Akhundi, A., Badiei, A., Ziarani, G.M., Habibi-Yangjeh, A., Muñoz-Batista, M.J., Luque, R., Graphitic carbon nitride-based photocatalysts: toward efficient organic transformation for value-added chemicals production. Mol. Catal.488 (2020) 110902.

[43] Moreira, N.F., Sampaio, M.J., Ribeiro, A.R., Silva, C.G., Faria, J.L., Silva, A.M., Metal-free g-C_3N_4 photocatalysis of organic micropollutants in urban wastewater under visible light. Appl. Catal. B: Environ. 248 (2019) 184-192.

[44] Mishra, A., Mehta, A., Basu, S., Shetti, N.P., Reddy, K.R., Aminabhavi, T.M., Graphitic carbon nitride (g–C_3N_4)-based metal-free photocatalysts for water splitting: a review, Carbon, 149 (2019) 693-721.

[45] Zhang, J., Chen, Y., Wang, X., Two-dimensional covalent carbon nitride nanosheets: synthesis, functionalization, and applications, Energy Environ. Sci. 8 (2015) 3092-3108.

[46] Hao, Q., Jia, G., Wei, W., Vinu, A., Wang, Y., Arandiyan, H., Ni, B.-J., Graphitic carbon nitride with different dimensionalities for energy and environmental applications, Nano Res. 13 (2020) 18-37.

[47] Darkwah, W.K., Ao, Y. Mini review on the structure and properties (photocatalysis), and preparation techniques of graphitic carbon nitride nano-based particle, and its applications, Nanoscale Res. Lett. 13 (2018) 1-15.

[48] Rono, N., Kibet, J.K., Martincigh, B.S., Nyamori, V.O., A review of the current status of graphitic carbon nitride, Crit. Rev. Solid State Mater. Sci. 46 (2021) 189-217.

[49] Liu, X., Ma, R., Zhuang, L., Hu, B., Chen, J., Liu, X., Wang, X., Recent developments of doped g-C_3N_4 photocatalysts for the degradation of organic pollutants, Crit. Rev. Environ. Sci. Technol.51(8) (2021) 751-790.

[50] Sudhaik, A., Khan, A.A.P., Raizada, P., Nguyen, V.-H., Van Le, Q., Asiri, A.M., Singh, P., Strategies based review on near-infrared light-driven bismuth nanocomposites for environmental pollutants degradation, Chemosphere, 291 (2021) 132781.

[51] Sang, Y., Liu, H., Umar, A., Photocatalysis from UV/Vis to near-infrared light: towards full solar-light spectrum activity, ChemCatChem, 7 (2015) 559-573.

[52] Zhou, B., Shi, B., Jin, D., Liu, X., Controlling upconversion nanocrystals for emerging applications, Nat. Nanotechnol. 10 (2015) 924-936.

[53] Wang, W., Ding, M., Lu, C., Ni, Y., Xu, Z., A study on upconversion UV–vis–NIR responsive photocatalytic activity and mechanisms of hexagonal phase $NaYF_4$: Yb^{3+}, Tm^{3+}@ TiO_2 core–shell structured photocatalyst, Appl. Catal. B: Environ. 144 (2014) 379-385.

[54] Lee, S.Y., Lee, G., Jun, Y.-S., Park, Y.I., Visible/near-infrared driven highly efficient photocatalyst based on upconversion nanoparticles/g-C_3N_4 nanocomposite, Appl. Surf. Sci. 508 (2020) 144839.

[55] Feng, L., He, F., Liu, B., Yang, G., Gai, S., Yang, P., Li, C., Dai, Y., Lv, R., Lin, J., g-C_3N_4 coated upconversion nanoparticles for 808 nm near-infrared light triggered phototherapy and multiple imaging, Chem. Mater. 28 (2016) 7935-7946.

[56] Liu, Y., Meng, X., Bu, W., Upconversion-based photodynamic cancer therapy, Coord. Chem. Rev. 379 (2019) 82-98.

[57] Singh-Rachford, T.N., Castellano, F.N., Photon upconversion based on sensitized triplet–triplet annihilation, Coord. Chem. Rev. 254 (2010) 2560-2573.

[58] Zhu, Y., Zheng, X., Lu, Y., Yang, X., Kheradmand, A., Jiang, Y., Efficient

upconverting carbon nitride nanotubes for near-infrared-driven photocatalytic hydrogen production, Nanoscale, 11 (2019) 20274-20283.

[59] Han, S., Deng, R., Xie, X., Liu, X., Enhancing luminescence in lanthanide-doped upconversion nanoparticles, Angew. Chem. Int. Ed. 53 (2014) 11702-11715.

[60] Huang, M.Z., Yuan, B., Dai, L., Fu, M.L., Toward NIR driven photocatalyst: Fabrication, characterization, and photocatalytic activity of β-$NaYF_4$: Yb^{3+}, Tm^{3+}/g-C_3N_4 nanocomposite, J. Colloid Interface Sci. 460 (2015) 264-272.

[61] Zhou, J., Liu, Q., Feng, W., Sun, Y., Li, F., Upconversion luminescent materials: advances and applications, Chem. Rev. 115 (2015) 395-465.

[62] Li, X., Zhang, F., Zhao, D., Lab on upconversion nanoparticles: optical properties and applications engineering via designed nanostructure, Chem. Soc. Rev. 44 (2015) 1346-1378.

[63] Bingham, S., Daoud, W.A., Recent advances in making nano-sized TiO_2 visible-light active through rare-earth metal doping, J. Mater. Chem. 21 (2011) 2041-2050.

[64] Eliseeva, S.V., Bünzli, J.C.G., Lanthanide luminescence for functional materials and bio-sciences, Chem. Soc. Rev. 39 (2010) 189-227.

[65] Gai, S., Li, C., Yang, P., Lin, J., Recent progress in rare earth micro/nanocrystals: soft chemical synthesis, luminescent properties, and biomedical applications, Chem. Rev. 114 (2014) 2343-2389.

[66] Auzel, F., Upconversion and anti-stokes processes with f and d ions in solids, Chem. Rev. 104 (2004) 139-174.

[67] Wenger, O.S., Güdel, H.U., Broadband near-infrared sensitization of visible upconversion luminescence in V^{3+} and Mo^{3+} co-doped Cs_2NaYCl_6, J. Phys. Chem. B, 106 (2002) 10011-10019.

[68] Amao, Y., Shuto, N., Furuno, K., Obata, A., Fuchino, Y., Uemura, K., Kajino,T., Sekito, T., Iwai, S., Miyamoto, Y., Artificial leaf device for solar fuel production, Faraday Discuss. 155 (2012) 289-296.

[69] Renero-Lecuna, C., Martín-Rodríguez, R., Valiente, R., González, J., Rodríguez, F., Kramer, K., Gudel, H., Origin of the high upconversion green luminescence efficiency in β-$NaYF_4$: 2% Er^{3+}, 20% Yb^{3+}, Chem. Mater. 23 (2011) 3442-3448.

[70] Wenger, O.S., Gamelin, D.R., Güdel, H.U., Chemical modification of transition metal upconversion properties: exchange enhancement of Ni^{2+} upconversion rates in Ni^{2+}: $RbMnCl_3$, J. Am. Chem. Soc. 122 (2000) 7408-7409.

[71] Gamelin, D.R., Güdel, H.U., Two-photon spectroscopy of d^3 transition metals: near-IR-to-visible upconversion luminescence by Re^{4+} and Mo^{3+}, J. Am. Chem. Soc. 120 (1998) 12143-12144.

[72] Chen, G., Ohulchanskyy, T.Y., Kumar, R., Ågren, H., Prasad, P.N., Ultrasmall monodisperse $NaYF_4$: Yb^{3+}/Tm^{3+} nanocrystals with enhanced near-infrared to near-infrared upconversion photoluminescence, ACS Nano, 4 (2010) 3163-3168.

[73] Suyver, J., Grimm, J., Krämer, K., Güdel, H.-U., Highly efficient near-infrared to visible up-conversion process in $NaYF_4$: Er^{3+}, Yb^{3+}, J. Lumin. 114 (2005) 53-59.

[74] Heer, S., Kömpe, K., Güdel, H.U., Haase, M., Highly efficient multicolour upconversion emission in transparent colloids of lanthanide-doped $NaYF_4$ nanocrystals, Adv. Mater. 16 (2004) 2102-2105.

[75] Xu, J., Brenner, T.J., Chen, Z., Neher, D., Antonietti, M., Shalom, M., Upconversion-agent induced improvement of g-C_3N_4 photocatalyst under visible light, ACS Appl. Mater. Interfaces, 6 (2014) 16481-16486.

[76] Yang, C., Zhao, W., Yu, X., Liu, H., Liu, J., Van Deun, R., Liu, Z., Facile synthesis and luminescence property of core-shell structured $NaYF_4$: Yb, Er/g-C_3N_4 nanocomposites, Mater. Res. Bull. 94 (2017) 415-422.

[77] Lu, X., Chen, F., Qian, J., Fu, M., Jiang, Q., Zhang, Q., Facile fabrication of CeF_3/g-C_3N_4 heterojunction photocatalysts with upconversion properties for enhanced photocatalytic desulfurization performance, J. Rare Earths. 39 (2021) 1204-1210.

[78] Turshatov, A., Busko, D., Baluschev, S., Miteva, T., Landfester, K., Micellar carrier for triplet–triplet annihilation-assisted

photon energy upconversion in a water environment, New J. Phys. 13 (2011) 083035.

[79] Parker, C., Hatchard, C., Sensitised anti-stokes delayed fluorescence, Proc. Chem. Soc. Lond. (1962) 386.

[80] Islangulov, R.R., Kozlov, D.V., Castellano, F.N., Low power upconversion using MLCT sensitizers, Chem. Commun. (2005) 3776-3778.

[81] Fang, J., Chen, Y., Wang, W., Fang, L., Lu, C., Zhu, C., Kou, J., Ni, Y., Xu, Z., Highly efficient photocatalytic hydrogen generation of g-C_3N_4-CdS sheets based on plasmon-enhanced triplet–triplet annihilation upconversion, Appl. Catal. B: Environ. 258 (2019) 117762.

[82] Xia, X., Deng, N., Cui, G., Xie, J., Shi, X., Zhao, Y., Wang, Q., Wang, W., Tang, B., NIR light induced H_2 evolution by a metal-free photocatalyst, Chem. Commun. 51 (2015) 10899-10902.

[83] Tyagi, A., Tripathi, K.M., Singh, N., Choudhary, S., Gupta, R.K., Green synthesis of carbon quantum dots from lemon peel waste: applications in sensing and photocatalysis, RSC Adv. 6 (2016) 72423-72432.

[84] Han, X., Han, Y., Huang, H., Zhang, H., Zhang, X., Liu, R., Liu, Y., Kang, Z., Synthesis of carbon quantum dots/SiO_2 porous nanocomposites and their catalytic ability for photo-enhanced hydrocarbon selective oxidation, Dalton Trans. 42 (2013) 10380-10383.

[85] Liu, S., Cao, H., Wang, Z., Tu, W., Dai, Z., Label-free photoelectrochemical cytosensing via resonance energy transfer using gold nanoparticle-enhanced carbon dots, Chem. Commun. 51 (2015) 14259-14262.

[86] Jiang, D., Zhang, Y., Chu, H., Liu, J., Wan, J., Chen, M., N-doped graphene quantum dots as an effective photocatalyst for the photochemical synthesis of silver deposited porous graphitic C_3N_4 nanocomposites for nonenzymatic electrochemical H_2O_2 sensing, RSC Adv. 4 (2014) 16163-16171.

[87] Gao, X., Lu, Y., Zhang, R., He, S., Ju, J., Liu, M., Li, L., Chen, W., One-pot synthesis of carbon nanodots for fluorescence turn-on detection of Ag^+ based on the Ag^+-induced enhancement of fluorescence, J. Mater. Chem. C, 3 (2015) 2302-2309.

[88] Jahanbakhshi, M., Habibi, B., A novel and facile synthesis of carbon quantum dots via salep hydrothermal treatment as the silver nanoparticles support: Application to electroanalytical determination of H_2O_2 in fetal bovine serum, Bioelectronics, 81 (2016) 143-150.

[89] Yu, H., Zhao, Y., Zhou, C., Shang, L., Peng, Y., Cao, Y., Wu, L.-Z., Tung, C.-H., Zhang, T., Carbon quantum dots/TiO_2 composites for efficient photocatalytic hydrogen evolution, J. Mater. Chem. A, 2 (2014) 3344-3351.

[90] Zhang, X., Wang, F., Huang, H., Li, H., Han, X., Liu, Y., Kang, Z., Carbon quantum dot sensitized TiO_2 nanotube arrays for photoelectrochemical hydrogen generation under visible light, Nanoscale, 5 (2013) 2274-2278.

[91] Amjadi, M., Abolghasemi-Fakhri, Z., Hallaj, T., Carbon dots-silver nanoparticles fluorescence resonance energy transfer system as a novel turn-on fluorescent probe for selective determination of cysteine, J. Photochem. Photobiol. A: Chem. 309 (2015) 8-14.

[92] Tian, J., Leng, Y., Zhao, Z., Xia, Y., Sang, Y., Hao, P., Zhan, J., Li, M., Liu, H., Carbon quantum dots/hydrogenated TiO_2 nanobelt heterostructures and their broad spectrum photocatalytic properties under UV, visible, and near-infrared irradiation, Nano Energy, 11 (2015) 419-427.

[93] Zhang, X., Huang, H., Liu, J., Liu, Y., Kang, Z., Carbon quantum dots serving as spectral converters through broadband upconversion of near-infrared photons for photoelectrochemical hydrogen generation, J. Mater. Chem. A, 1 (2013) 11529-11533.

[94] Hassan, M., Gomes, V.G., Dehghani, A, Ardekani, S.M., Engineering carbon quantum dots for photomediated theranostics, Nano Res. 11 (2018) 1-41.

[95] Zhu, S., Song, Y., Zhao, X., Shao, J., Zhang, J., Yang, B., The photoluminescence mechanism in carbon dots (graphene quantum dots, carbon nanodots, and polymer dots): current state and future perspective, Nano Res. 8 (2015) 355-381.

[96] Yu, H., Shi, R., Zhao, Y., Waterhouse, G.I., Wu, L.Z., Tung, C.H., Zhang, T., Smart utilization of carbon dots in semiconductor

photocatalysis, Adv. Mater. 28 (2016) 9454-9477.

[97] Liu, Q., Chen, T., Guo, Y., Zhang, Z., Fang, X., Ultrathin g-C_3N_4 nanosheets coupled with carbon nanodots as 2D/0D composites for efficient photocatalytic H_2 evolution, Appl. Catal. B: Environ. 193 (2016) 248-258.

[98] Feng, C., Deng, Y., Tang, L., Zeng, G., Wang, J., Yu, J., Liu, Y., Peng, B., Feng, H., Wang, J., Core-shell Ag_2CrO_4/N-GQDs@ g-C_3N_4 composites with anti-photocorrosion performance for enhanced full-spectrum-light photocatalytic activities, Appl. Catal. B: Environ. 239 (2018) 525-536.

[99] Che, H., Liu, C., Hu, W., Hu, H., Li, J., Dou, J., Shi, W., Li, C., Dong, H., NGQD active sites as effective collectors of charge carriers for improving the photocatalytic performance of Z-scheme g-C_3N_4/Bi_2WO_6 heterojunctions, Catal. Sci. Technol. 8 (2018) 622-631.

[100] Zhao, F., Khaing, K.K., Yin, D., Liu, B., Chen, T., Wu, C., Huang, K., Deng, L., Li, L., Large enhanced photocatalytic activity of g-C_3N_4 by fabrication of a nanocomposite with introducing upconversion nanocrystal and Ag nanoparticles, RSC Adv. 8 (2018) 42308-42321.

[101] Murali, G., Vattikuti, S.P., Kshetri, Y.K., Lee, H., Modigunta, J.K.R., Reddy, C.S., Park, S., Lee, S., Poornaprakash, B., Lee, H., Near-infrared-activated Z-scheme $NaYF_4$:Yb/Tm@Ag_3PO_4/Ag@g-C_3N_4 photocatalyst for enhanced H_2 evolution under simulated solar light irradiation, Chem. Eng. J. 421 (2021) 129687.

[102] Wang, W., Jimmy, C.Y., Shen, Z., Chan, D.K., Gu, T., g-C_3N_4 quantum dots: direct synthesis, upconversion properties and photocatalytic application, Chem. Commun. 50 (2014) 10148-10150.

[103] Huang, Z., Chen, H., Zhao, L., He, X., Du, Y., Fang, W., Li, W., Tian, P., Constructing g-C_3N_4 quantum dots modified g-C_3N_4/GO nanosheet aerogel for UV-Vis-NIR driven highly efficient photocatalytic H_2 production, Int. J. Hydrog. Energy. 44 (2019) 31041-31052.

[104] Qin, J., Zeng, H., Photocatalysts fabricated by depositing plasmonic Ag nanoparticles on carbon quantum dots/graphitic carbon nitride for broad spectrum photocatalytic hydrogen generation, Appl. Catal. B: Environ. 209 (2017) 161-173.

[105] Zhang, Q., Deng, J., Xu, Z., Chaker, M., Ma, D., High-efficiency broadband C_3N_4 photocatalysts: synergistic effects from upconversion and plasmons, ACS Catal. 7 (2017) 6225-6234.

[106] Zhang, C., Fu, Z., Hong, F., Pang, G., Dong, T., Zhang, Y., Liu, G., Dong, X., Wang, J., Non-metal group doped g-C_3N_4 combining with BiF_3: Yb^{3+}, Er^{3+} upconversion nanoparticles for photocatalysis in UV–Vis–NIR region, Colloid. Surf. A: Physicochem. Eng. Asp. 627 (2021) 127180.

[107] Liang, S., He, M., Guo, J., Yue, J., Pu, X., Ge, B., Li, W., Fabrication and characterization of BiOBr:Yb^{3+}, Er^{3+}/g-C_3N_4 p-n junction photocatalysts with enhanced visible-NIR-light-driven photoactivities, Sep. Purif. Technol. 206 (2018) 69-79.

[108] Cheng, E., Zhou, S., Li, M., Li, Z., Synthesis of g-C_3N_4-based $NaYF_4$:Yb,Tm@TiO_2 ternary composite with enhanced Vis/NIR-driven photocatalytic activities, Appl. Surf. Sci. 410 (2017) 383-392.

[109] Zhang, M., Zhang, Y., Tang, L., Zeng, G., Wang, J., Zhu, Y., Feng, C., Deng, Y., He, W., Ultrathin Bi_2WO_6 nanosheets loaded g-C_3N_4 quantum dots: A direct Z-scheme photocatalyst with enhanced photocatalytic activity towards degradation of organic pollutants under wide spectrum light irradiation, J. Colloid Interface Sci. 539 (2019) 654-664.

[110] Feng, S., Chen, T., Liu, Z., Shi, J., Yue, X., Li, Y., Z-scheme CdS/CQDs/g-C_3N_4 composites with visible-near-infrared light response for efficient photocatalytic organic pollutant degradation, Sci. Total Environ. 704 (2020) 135404.

List of Abbreviations

Apparent quantum efficiency (AQE); Carbon quantum dots (CQDs); Charge transfer (CT); Ciprofloxacin (CIP); Conduction band (CB); Cooperative upconversion (CU); Cross relaxation (CR), Density functional theory (DFT); Density of states (DOS); Dibenzothiophene (DBT); Diethylamine (DEA); Diffuse reflectance spectra (DRS); Energy transfer (ET); Energy transfer upconversion (ETU); Excited state (ES); F¨orster resonance energy transfer (FRET); Ground state (GS); Intermediate excited state (IES); Internal electric field (IEF); Intersystem crossing (ISC); Lanthanides (Ln); Methyl orange (MO); Methylene blue (MB); Nanocrystals (NCs); Nanorods (NRs); Nanosheets (NSs); Nanotubes (NT); Near-infrared (NIR); Nanoparticles (NPs); Oxygen vacancies (OVs); Oxytetracycline (OTC); Phonon avalanche (PA); Photoluminescence (PL); Reactive oxygen species (ROS); Rhodamine B (RhB); Successive energy transfer (SET); Surface plasmon resonance (SPR); Tetracycline (TC); Triplet-Triplet Annihilation (TTA); Triplet-triplet energy transfer (TTET); Upconversion (UC); Upconversion luminescence (UCL); Upconversion nanocrystals (UC NCs); Upconversion nanoparticles (UC NPs); Ultraviolet (UV); Valence band (VB)